The prion-like domain of the chloroplast RNA binding protein CP29A is required for cold-induced phase separation next to nucleoids and supports RNA splicing and translation during cold acclimation

Julia Legen[1$], Benjamin Lenzen[1$], Nitin Kachariya[2,3], Stephanie Feltgen[1], Yang Gao[4], Simon Mergenthal[5], Willi Weber[5], Enrico Klotzsch[5], Reimo Zoschke[3], Michael Sattler[2,3], Christian Schmitz-Linneweber[1]

[1] Molecular Genetics, Humboldt Universität zu Berlin, Philippstr.13, 10115 Berlin, Germany.

[2] Helmholtz Munich, Institute of Structural Biology, Ingolstädter Landstrasse 1, 85764, Germany

[3] Technical University of Munich, TUM School of Natural Sciences, Department of Bioscience, Bavarian NMR Center, Lichtenbergstr. 4, 85747 Garching, Germany.

[4] Max Planck Institute of Molecular Plant Physiology, Am Mühlenberg 1, 14476 Potsdam-Golm, Germany

[5] Institute for Biology, Experimental Biophysics/Mechanobiology, Humboldt-Universität zu Berlin, Invalidenstraße 42, 10115 Berlin, Germany

Corresponding author: christian.schmitz-linneweber@rz.hu-berlin.de

[$] equal contribution

Abstract

Arabidopsis thaliana is capable of producing photosynthetic tissue with active chloroplasts at temperatures as low as 4°C, and this process depends on the presence of the nuclear-encoded, chloroplast-localized RNA-binding protein CP29A. In this study, we demonstrate that CP29A undergoes phase separation in vitro and in vivo in a temperature-dependent manner, which is mediated by a prion-like domain (PLD) located between the two RNA recognition motif (RRM) domains of CP29A. The resulting droplets display liquid-like properties and are found in close proximity to chloroplast nucleoids. The PLD is required to support chloroplast RNA splicing and

1

32 translation in cold-treated tissue. Together, our findings suggest that plant chloroplast
33 gene expression is compartmentalized by inducible condensation of CP29A at low
34 temperatures, a mechanism that could play a crucial role for plant cold resistance.

Introduction

36 Phase separation (PS) is a phenomenon that can lead to the formation of
37 membraneless compartments within cells (Shin and Brangwynne, 2017). These
38 compartments are a dynamic alternative to organelles, as they lack a physical,
39 membranous boundary and can be modulated by changes in protein concentrations,
40 metabolites, salt or temperature (Alberti and Hyman, 2021). Compartments induced by
41 PS are important for efficiently organizing cellular processes by concentrating specific
42 factors in their appropriate place and at the right time. Unlike irreversible cellular
43 aggregation, these compartments are dynamically formed and dissolved and have a
44 viscoelastic-dynamic, fluid nature, which makes them flexible and adaptable. PS has
45 been demonstrated to be crucial for rapid responses to changing environments, and
46 can be induced by shifts in temperature and cellular homeostasis (Nott et al., 2015;
47 Dignon et al., 2019). Intrinsically disordered protein domains (IDRs) are often at the
48 heart of PS phenomena, driving the formation of cellular membrane-less
49 compartments through multivalent interactions (Kato et al., 2012; Forman-Kay and
50 Mittag, 2013). RNA can act as a seed and essential component for phase-separated
51 compartments, with RNA-binding proteins being over-represented among factors
52 described to phase-separate (Roden and Gladfelter, 2021). PS and the resulting RNA
53 granules play a crucial role in a number of processes involving RNA binding proteins,
54 including ribosome maturation, RNA splicing, ribonucleoprotein biogenesis, and RNA
55 degradation.

56 In plants, PS phenomena are just beginning to be characterized (Emenecker et al.,
57 2020; Gutierrez-Beltran et al., 2023; Kang and Xu, 2023), but it is already clear that
58 condensates contribute to stress resilience and signaling (Field et al., 2023; Solis-
59 Miranda et al., 2023; Kearly et al., 2022). Almost all of the PS events described in land
60 plants occur in the cytosol or the cytoplasm (Jung et al., 2020; Xie et al., 2021; Fang
61 et al., 2019; Shang et al., 2023; Kim et al., 2021; Tan et al., 2023; Zavaliev et al., 2020;
62 Zhang et al., 2022; Huang et al., 2021b; Hoffmann et al., 2023; Wang et al., 2023;
63 Ruiz-Solaní et al., 2023), but there is one notable exception: In Arabidopsis
64 chloroplasts, an ankyrin protein has been shown to undergo phase separation to

2

65 facilitate sorting and transport of proteins into the thylakoids (Ouyang et al., 2020).
66 Phase separation also plays a role in chloroplasts of green algae, where the chloroplast
67 pyrenoid, a structure required for carbon concentration around RuBisCo, has been
68 shown to assemble via condensation (Freeman Rosenzweig et al., 2017). There are
69 also reports of RNA granules in the chloroplast of a green alga, but whether they are
70 based on PS phenomena is unclear (Uniacke and Zerges, 2009, 2008). Similarly, heat
71 inducible stress granules were observed in Arabidopsis chloroplasts, but the influence
72 of PS is unclear (Chodasiewicz et al., 2020).

73 The chloroplast RNA-binding protein CP29A is a member of the cpRNP protein family,
74 which has eleven representatives in Arabidopsis, all localizing to chloroplasts (Ruwe
75 et al., 2011). Unlike the other 10 family members, CP29A's two RNA recognition motifs
76 (RRMs) are spaced by a linker of 84 amino acids. CP29A responds to different external
77 and internal stimuli, accumulating to higher levels in the cold and being repressed by
78 other stressors and abscisic acid (Kupsch et al., 2012; Raab et al., 2006). CP29A
79 associates with a large number of chloroplast transcripts (Kupsch et al., 2012). A
80 homologue of CP29A in tobacco is required for stabilizing chloroplast RNAs in vitro
81 (Nakamura et al., 2001). Null mutants of CP29A exhibit a pale center of the leaf rosette
82 after long-term exposure to low temperatures, with defects in chloroplast RNA
83 processing and accumulation (Kupsch et al., 2012). When grown at regular growth
84 temperatures, CP29A-deficient plants do not show RNA defects or macroscopic
85 changes relative to wt plants, indicating that CP29A has evolved to support cold
86 acclimation in *Arabidopsis thaliana* (Kupsch et al., 2012). The temperature range in
87 which CP29A is relevant does not fall within the realm of stress, but rather within a
88 range that plants such as *A. thaliana* are constantly exposed to in temperate zones,
89 specifically from 4°C to 12°C. Therefore, CP29A is a factor that is crucial for the daily
90 acclimatization to low temperatures, which are to be expected throughout the year in
91 temperate regions. The molecular mechanisms by which CP29A achieves this
92 acclimatization of plastidic RNA metabolism and prevents bleaching remains unclear,
93 nor was it determined whether the effects on RNA maturation and accumulation
94 observed in pale tissue were of primary origin or are pleiotropic effects of the non-
95 photosynthetic tissue. We report here that CP29A is capable of forming liquid-like
96 droplets in vitro and in vivo via its prion-like domain (PLD) and that the PLD is required
97 for chloroplast splicing, translation and cold resistance.

Results

The organellar RNA-binding protein CP29A has a prion-like domain, which is required for phase separation in vitro

The protein CP29A contains two RNA recognition motifs (RRMs) that are separated by a linker domain consisting of 84 amino acids. This linker has a repetitive, low complexity sequence with charged and polar residues, and is intrinsically disordered with a prion-like amino acid composition according to *in silico predictions* using the PLAAC and the SPOTD tool (Figure 1A; Lancaster et al., 2014; Hanson et al., 2019). To determine whether CP29A can undergo phase separation, we used recombinant, purified CP29A and monitored its behavior at different temperatures. We found that the CP29A solution becomes turbid at low - but still physiological - temperatures within a few minutes but returns to full translucence when brought back to room temperature (Figure 1B). By contrast, the protein precipitates irreversibly when heated to 37°C (Figure 1B). Next, we analyzed whether full-length CP29A, the PLD alone or a PLD-deletion protein can form liquid droplets. For the PLD deletion, we removed 60 amino acids comprising the glycine-rich region, but still leaving a linker between the RRMs of 16 amino acids (Figure S1A). With the exception of CP29A, all other cpRNP family members have short linkers; for example CP28A has a linker of 18 residues and CP33B has 26 residues (Figure S1A). We reasoned that within this protein family, the two RRM domains are functional if distanced by a short linker, although we cannot exclude structural effects of the PLD deletion on the RRM domains. For visualization, we fused the different protein versions N-terminally to mNeongreen, while omitting the organellar-targeting sequence, since it is cleaved off in vivo. We expressed the protein variants in *E. coli* and purified them (Figure S1B). Indeed, mNeongreen::CP29A formed spherical liquid droplets and wetted the glass surface after settling to the bottom of the dish (Figure 1C; Movie S1). Droplet size increased over time and droplets started to coalesce, which is indicative of the liquid nature of the phase being formed (Figure 1D). Similarly, the PLD alone assembled droplets that fused, while the PLD-less CP29A protein formed irregularly shaped aggregates that did not show fusion (Figure 1D). To investigate the dynamics of mNeongreen::CP29A within droplets, we performed fluorescence recovery after photobleaching (FRAP) experiments. After high-intensity laser irradiation, fluorescence recovers with a halftime of 3.9±0.2 sec for

4

130   the full length protein, while PLD alone (5.3±0.4 sec) and CP29AΔPLD (9.9±0.7 sec)

131   recovery is slower (Figure 1E). Furthermore, CP29AΔPLD aggregates did not show full

132   recovery after photobleaching, but plateaued at 69 percent demonstrating low mobility

133   of proteins within this phase, while both full length and PLD CP29A showed a recovery

134   of greater than 95 percent (Figure 1E).

135   As anticipated, our results revealed a positive correlation between droplet formation

136   and protein concentration, as shown in Figure 1F for both the full-length and PLD-only

137   proteins. The PLD-only protein resulted in more droplets than the full-length protein at

138   lower protein concentrations (25 µM), while the PLD-less CP29A did show aggregates

139   at all concentrations assayed (Figure 1F). We also exposed the full-length protein to

140   low temperatures and observed that droplet size increased significantly in the cold

141   (Figure 1G), with an average diameter of 1.2 µm (±0.4 nm) at 21°C and 1.8 (±0.7) µm

142   at 4°C (n = 1497 and n = 197 droplets at 21°C and 4°C, respectively). We next tested

143   the impact of salt on droplet formation and found that concentrations of 100 mM and

144   150 mM facilitated droplet formation, while droplet-size decreased at higher salt

145   concentrations (Figure 1H). The negative impact of higher salt concentrations on the

146   full-length protein is also observed at low temperatures in turbidity assays (Figure S1C)

147   and can be interpreted as a suppression of intermolecular interactions by electrostatic

148   shielding. Taken together, these data established that CP29A undergoes phase

149   separation in vitro to form liquid droplets, which depends on its PLD and is supported

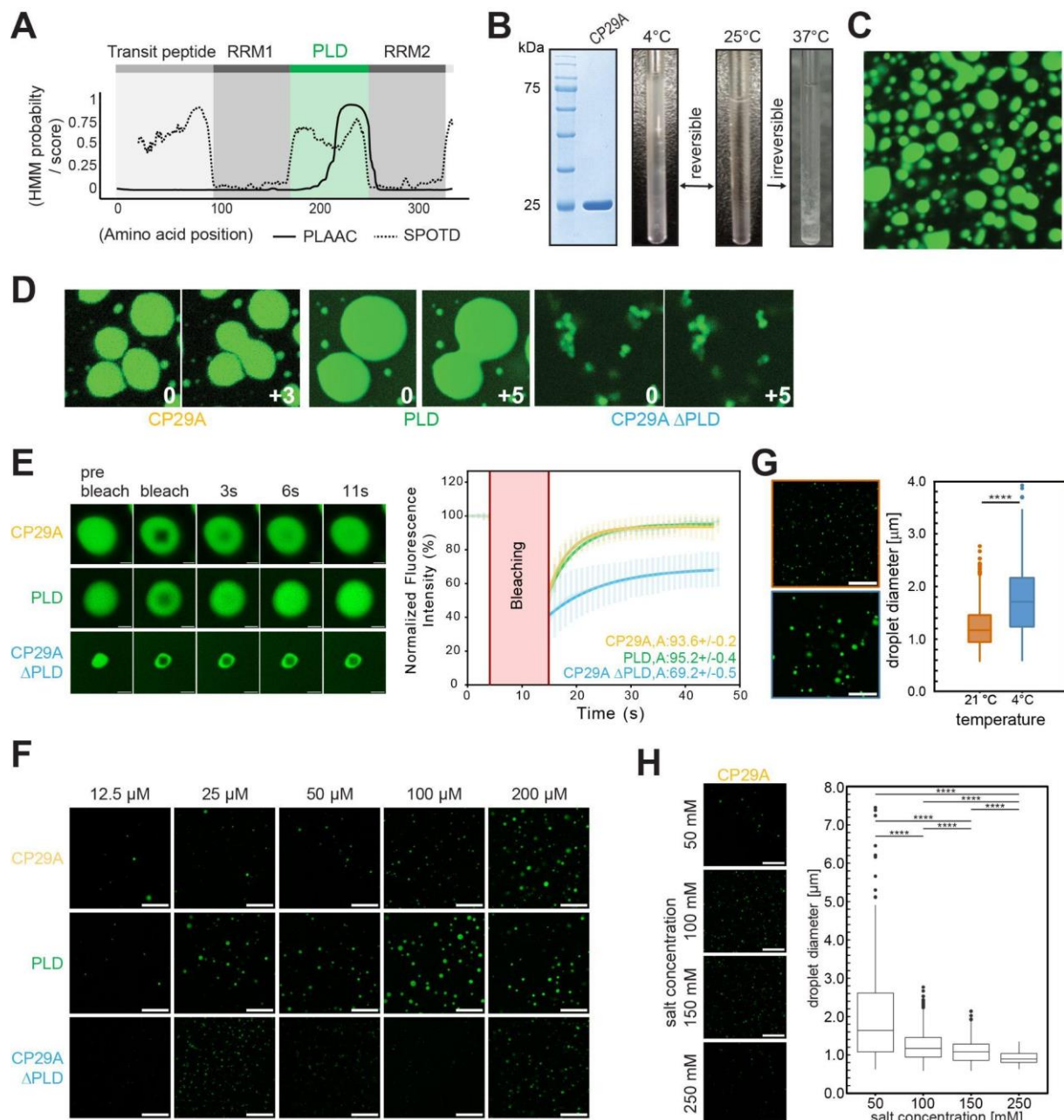150   by low temperatures.

151

152

Figure 1: CP29A forms condensates in vitro

(A) Schematic diagram of the CP29A protein with its two RRM domains. Below, results of disordered domain predictions within CP29A using the PLAAC and SpotD tools are shown. Scores for both predictors suggest disorderness in the linker between the two RRM domains, including a predicted prion-like domain.

(B) Left: Coomassie stain of purified recombinant CP29A excluding the signal peptide, separated by SDS-PAGE. Right: Glass vial with 80 µM CP29A solution is shifted between different temperatures to demonstrate reversible turbidity changes.

(C) In vitro phase-separation assay of 100 nM mNG::CP29A with 10% (w/v) PEG4000 treatment for 1 min prior to imaging; imaged with confocal microscopy.

(D) Fusion events of mNG::CP29A and mNG:::PLD droplets; conditions as in (C); numbers indicate seconds passed between frames shown; note that CP29AΔPLD forms aggregates that were never observed to fuse.

(E) Quantification of fluorescent recovery after photobleaching (FRAP) kinetics with mNG::CP29A, CP29AΔPLD and mNGPLD; all at 100 nM. Error bars = SD; Data are means of the fluorescence values from at least 10 experiments per protein. The images were taken every second over 40 to 50 s to document fluorescence recovery, each time point was normalized to the value before photobleaching. Note that the full-length protein and

6

the PLD recover at a very similar rate, while the PLD-less protein recovers much more slowly. A = plateau intensity as an indicator of the mobile protein fraction. Scale bar: 2 μm

(F) **Phase separation of mNG::CP29A, mNG:::PLD droplets and CP29AΔPLD at different protein concentrations, scale bar: 20 μm.** The experiment was performed three times; representative results are shown.

(G) **Microscopy of mnG::CP29A droplets (left) and their size distribution (right) of mNG::CP29A at 21°C and 4°C, respectively (50 μM protein; 100 mM NaCl), scale bar 20 μm.**

(H) **Microscopy of phase separation (left) and size distribution (right) of mNG::CP29A at different salt concentrations, scale bar: 20 μm.**

NMR analysis of CP29A indicates molecular interactions of the PLD within the condensed phase

Next, we utilized nuclear magnetic resonance (NMR) spectroscopy along with other biophysical methods in order to investigate the conformation of CP29A at residue level. We expressed and purified the individual RRM domains and the PLD linker and assigned the NMR backbone chemical shifts. Our analysis revealed that CP29A harbors two canonical RRM domains with β_1-α_1-β_2-β_3-α_2-β_4-β_5 and β_1-α_1-β_2-β_3-α_2-β_4 secondary structure for RRM1 and RRM2, respectively. Furthermore, NMR chemical shifts indicate that the PLD linker connecting the two RRMs is intrinsically disordered (Figure 2A and Figure S1B, D, E). Notably, the PLD linker of CP29A comprises low-complexity regions with repeats of serine (17%), arginine (9%), tyrosine (7%), and glutamate (6%; Figure 2B, Figure S1A), which can potentially engage in electrostatic and cation-π interactions and is rich in glycines (34%; Figure 2B). These features can mediate interactions in phase-separated condensates (Wang et al., 2018b; Qamar et al., 2018). To study the phase separation potential of CP29A in detail, we monitored changes of full length CP29A at temperatures ranging from 298K to 275K in NMR fingerprint spectra. Extensive line-broadening of amide signals was observed at lower temperatures, consistent with reduced molecular tumbling of the protein in a disperse phase (Figure 2C, D; Figure 1B). The extent of line-broadening was significantly larger than expected from the temperature dependence of the molecular tumbling, suggesting that it is due to molecular interactions in the condensed phase.

Since the PLD linker is responsible for phase separation of CP29A (Figure 1), we purified the PLD alone and analyzed its biophysical properties (Figure 2E; Figure S1B, D middle panel). By lowering the temperature, noticeable line-broadening of amide

208   signals was observed, similar to the full-length protein, consistent with reduced mobility
209   and condensate formation in disperse solution (Figure 2F, G upper panel). To
210   investigate the conformational dynamics of the PLD in solution, {^{1}H}-^{15}N heteronuclear
211   nuclear Overhauser effect (hetNOE) experiments were performed at 298K and 275K.
212   These data demonstrate that the PLD has overall reduced backbone flexibility at sub-
213   nanosecond time scales at lower temperature with pronounced rigidification for
214   glycines and serines between residues 245-254 (Figure 2G lower panel). The overall
215   flexibility of the PLD is also seen in a Kratky plot derived from small-angle X-ray
216   scattering (SAXS; Figure S2A). The pairwise-distance distribution suggests a broad
217   range of conformations of the protein up to 100 Å pairwise distances, indicating that
218   the PLD dynamically samples a wide range of conformations in solution (Figure S2B,
219   C; Table S1). In summary, the low complexity region of the PLD of CP29A is
220   unstructured, flexible and undergoes temperature-dependent phase separation similar
221   to previously characterized known PLDs (Franzmann and Alberti, 2019; Wang et al.,
222   2018b).

223   To confirm that the observed NMR line-broadening reflects reduced tumbling in the
224   condensed phase based on intermolecular interactions, we conducted an NMR titration
225   of ^{15}N-labeled PLD with unlabeled PLD at lower temperature (Figure 2H, I). Changes
226   in ^{15}N amide chemical shifts and line-broadening, reflected by an 2.2-fold intensity
227   reduction.2 upon the addition of 40-fold molar excess of unlabeled PLD protein,
228   indicated that the ^{15}N-labeled protein participates in phase separation with the
229   unlabeled protein in a condensed phase. The most prominent NMR spectral changes
230   are observed for the Gly-Tyr-Gly-Ser-Glu-Arg-Gly-Gly repeats, consistent with weak
231   electrostatic intermolecular interactions (Figure 2J). In sum, our NMR analysis
232   demonstrates high flexibility of the PLD in free solution, which is reduced at lower
233   temperatures consistent with charged interactions that contribute to condensed phase
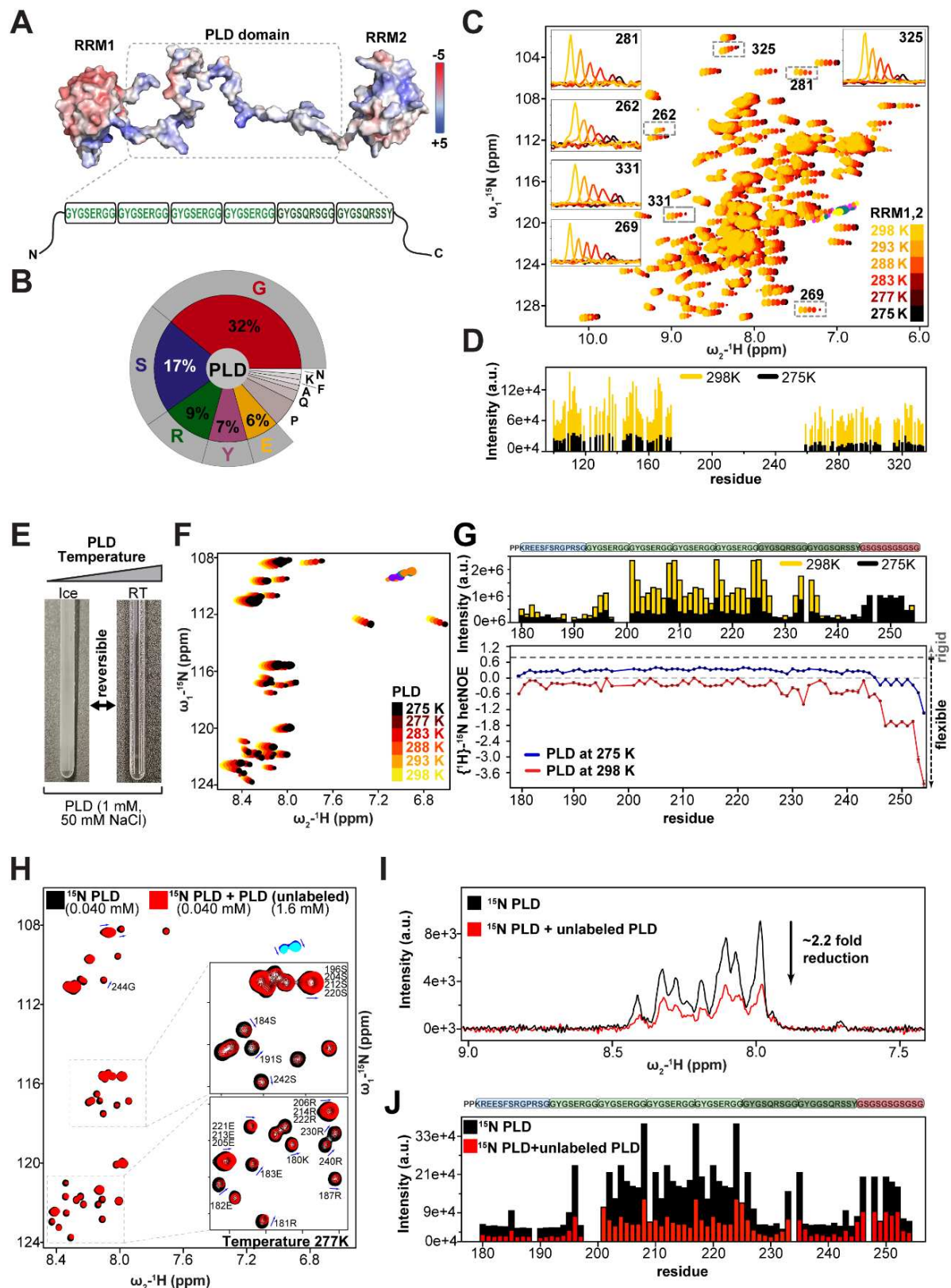234   formation.

235

Figure 2: Temperature dependent biophysical characterization of tandem RRMs and the PLD linker of CP29A.

> **(A)** Structural model of tandem RRMs of CP29A with electrostatic surface potential rendering (positive (blue) to negative (red) in [kJ/mol/e] as indicated) and the primary sequence of its PLD linker. Repeated sequence elements are boxed.
> **(B)** Pie-chart shown for the PLD domain with the proportion of each amino acid.
> **(C)** Overlay of ^1H, ^{15}N HSQC spectra of 90 μM concentration of tandem RRMs of CP29A measured at different temperatures. The inset shows the line-broadening with 1D slices of the cross peaks in the 2D experiment upon temperature shift from 298K to 275K.
> **(D)** Boxplot for signal intensities of amide protons for spectra shown in figure (C) at 298K (yellow) and at 275K (black).
> **(E)** Turbidity changes of a 50 mM PLD solution upon change from ice to room temperature.
> **(F)** Overlay of a series of ^1H, ^{15}N HSQC spectra of the PLD linker with increasing temperature from 275K to 298K. Line-broadening of NMR signals is observed at 275K and 277K.
> **(G)** Upper panel : Box plot of the intensity of amide proton signals in (F) at 298K and 275K, in yellow and black color, respectively. Lower panel: Comparison of $\{^1H\}$-^{15}N heteronuclear NOE of the PLD at 298K and 277K shown in red and blue, respectively.
> **(H)** Overlay spectra of the ^{15}N labeled PLD alone (black) and in presence of 40-fold excess of unlabeled PLD (red) measured at 277K. Blue arrows indicate smallchemical shift changes.
> **(I)** Overlay of 1D amide proton signals for the samples and conditions shown in figure (H). Intensity reduction of the signals is indicated with an arrow.
> **(J)** Box plot for signal intensities in the spectra shown in figure (H).

CP29A localizes to granules proximal to nucleoids in vivo

We next investigated the potential of CP29A to undergo phase separation within plant chloroplasts. We generated plant lines that express mGFP fused to full-length CP29A (mGFP::CP29Afl), and CP29A without its PLD (mGFP::CP29AΔPLD), both in a *cp29a* null mutant background. The expression of both constructs was driven by the native CP29A promoter, and their expression levels were comparable (Figure S3A). Protoplasts from the mGFP::CP29Afl lines exhibited punctate signals when analyzed by confocal microscopy, which increased in number over time when incubated at 8°C, while protoplasts from the mGFP::CP29AΔPLD plant lines showed much fewer granular signals (Figure 3A). These findings suggest that the PLD of CP29A is strongly supportive of efficient droplet formation in vivo*,* but also shows that recruitment into granular structures is still possible for the truncated CP29A protein albeit at much lower efficiency. Furthermore, our data indicate that low temperatures not only promote droplet formation in vitro but also in living cells.

We next investigated whether the formation of CP29A droplets is linked to nucleoids, given that nucleoids contain a large number of RNA binding proteins (Majeran et al. 2011). To answer this question, we utilized STED microscopy, which is better equipped

10

277 to resolve the suborganellar distribution of CP29A droplets and DAPI-stained nucleoids
278 than standard confocal microscopy. Our observations indicated that the GFP signal
279 and the DAPI signal only occasionally overlap (Figure 3B). However, we frequently
280 observed that the two signals appeared as doublets (Figure 3B arrowheads),
281 prompting us to explore the possibility of a physical connection between CP29A
282 droplets and nucleoids, similar to the known tethering of mitochondrial RNA droplets
283 to nucleoids (Rey et al., 2020; Antonicka and Shoubridge, 2015). By measuring the
284 distance between nucleoids and CP29A droplets, we discovered a non-random
285 distribution of the two signals, with an average distance of 0.2 µm (Figure 3C). As a
286 control, we examined whether a modeled random distribution of nucleoids and CP29A
287 droplets would result in a similar distance. For that we estimated average numbers of
288 nucleoids and CP29A droplets from fluorescence images and found that a random
289 distribution of the two signals in the chloroplast volume led to an average distance of
290 0,488 µm, which was significantly larger than the distance measured in the in vivo data
291 (Figure 3D).

292 To validate our findings using an alternative detection method of CP29A droplets, we
293 employed the SNAP tag, which is also more suitable for STED microscopy since it
294 allows the usage of organic dyes that emit two orders of magnitude more photons than
295 GFP (Dempsey et al., 2011; Fernández-Suárez and Ting, 2008) We generated plants
296 that stably express CP29A with an N-terminal SNAP-tag in a *cp29a* mutant
297 background, as well as plants expressing SNAP::CP29AΔPLD in the same
298 background. The expression levels were comparable between both lines and slightly
299 higher than in wt (Figure S3B). We generated protoplasts from both SNAP::CP29Afl
300 and SNAP::CP29AΔPLD lines and incubated them with the SNAP-compatible dye Cell-
301 SiR647 for one hour. As seen in the mGFP::CP29A expressing plants, only the lines
302 expressing full-length CP29A exhibited a granular localization of CP29A, while the
303 plants lacking the PLD showed a diffuse signal with few granular bodies (Figure 3E).
304 Consistent with our observations in GFP-tagged lines, we also found a correlation
305 between the location of CP29A signal and nucleoids in SNAP::CP29Afl protoplasts
306 (Figure 3F), with an average distance of the two signals of 0.24 µm. These findings
307 demonstrate that droplet formation occurs in living chloroplasts and is not reliant on
308 the tags utilized, as both GFP- and SNAP-tagged CP29A form droplets. Moreover, our

11

309   results provide compelling evidence that CP29A droplets are in close proximity to
310   nucleoids.

311   To further corroborate our findings, we performed immunofluorescence assays on wild
312   type (wt) protoplasts using an antibody against the native CP29A protein. Since the
313   antibody was designed to recognize the PLD region, it could only be used for analysis
314   of plants expressing full-length CP29A. Consistent with our GFP- and SNAP-tagged
315   fusion protein experiments, immunofluorescence assays revealed granular signals that
316   increased in number at low temperatures (Figure S4). We observed that the granular
317   signals were mainly located near the chloroplast envelope, potentially due to limitations
318   in the antibody's ability to penetrate formaldehyde-fixed chloroplasts densely packed
319   with thylakoid membranes. Importantly, this analysis demonstrates that droplet
320   formation of CP29A is not an artifact of transgene overexpression or fusion protein
321   production.

322   To exclude that granule formation is induced by protoplastation, we next investigated
323   leaf tissue for the localization of mGFP::CP29Afl and mGFP::CP29AΔPLD. Starting
324   with material grown entirely at 21°C, we saw very few granular structures in
325   chloroplasts of either genotype (Figure 3G). When the plant material was however
326   transferred to 12°C, the signals became more punctate in mGFP::CP29Afl plants.
327   These signals were no in all cases roundish, possibly restricted and deformed by the
328   thylakoid membrane system. In some mGFP::CP29Afl cells, chloroplasts were replete
329   with granules. Structures with higher signal density were also found in chloroplasts
330   from mGFP::CP29AΔPLD leaves, but in much lower numbers (Figure 3H). Taken
331   together, our analyses provide strong evidence that CP29A forms droplets near
332   nucleoids in living cells, and that this behavior is strongly supported by the PLD region
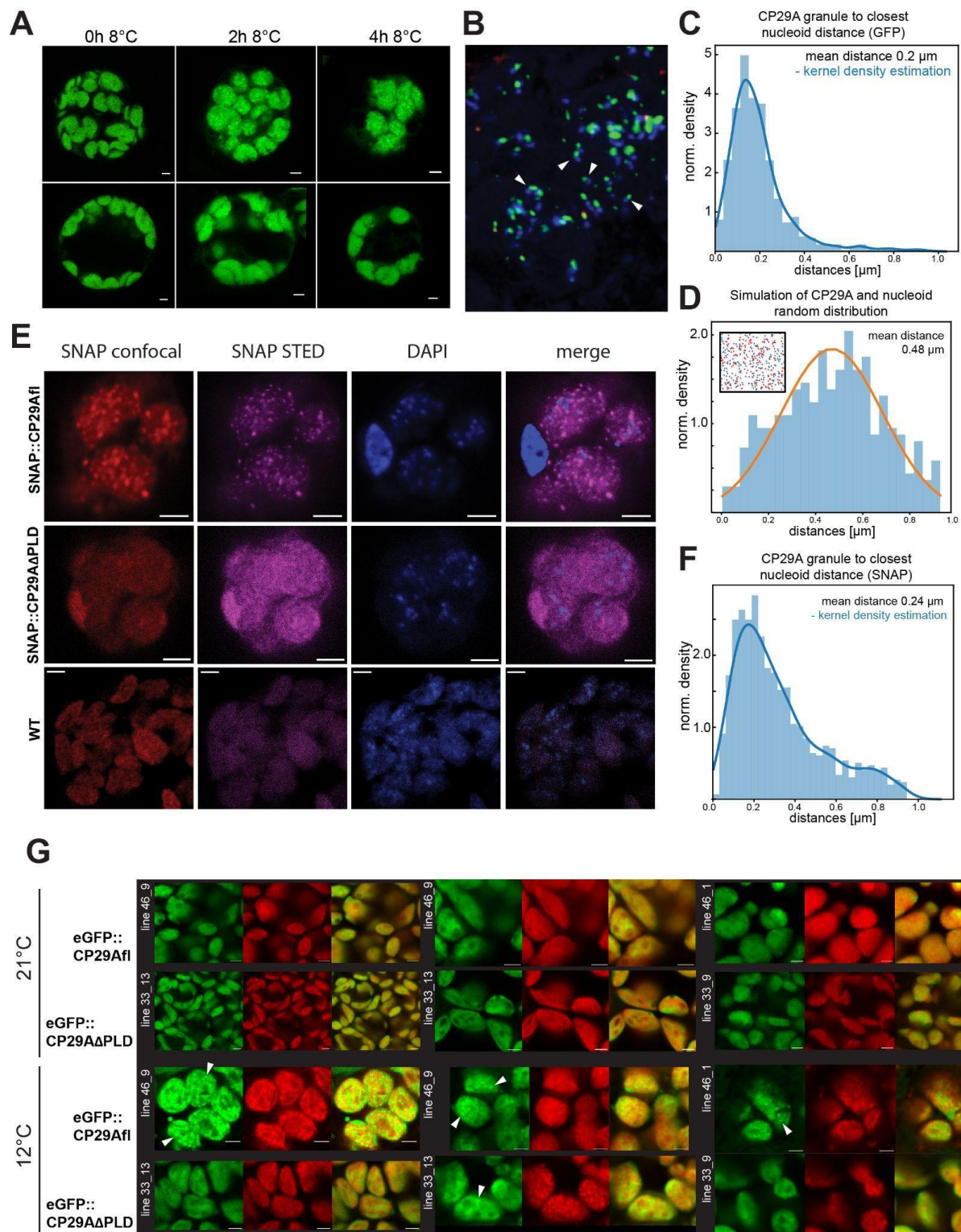333   and is promoted by low temperatures.

Figure 3: CP29A forms droplets in the vicinity of nucleoids, which depends on its PLD and is fostered by low temperatures

(A) Confocal microscopy of protoplasts prepared from wt and the transgenic lines stably expressing mGFP::CP29Afl or mGFP::CP29AΔPLD, exposed to low temperature for the indicated time. Scale bar: 10 μm. Three replicates were performed with independent transgenic lines for each genotype.

(B) STED microscopy of protoplasts expressing full-length CP29A fused to GFP and stained with DAPI. Arrowheads point to examples of doublet signals.

(C) Quantification of the distance of CP29A droplets and nucleoids in (B).

13

344 **(D) Simulation of a random distribution of CP29A droplets and nucleoids based on the**
345 **number of signals in (B) per volume analyzed.**
346 **(E) Confocal and STED microscopy of protoplasts prepared from transgenic lines stably**
347 **expressing SNAP::CP29Afl or SNAP::CP29A ΔPLD and exposed to low temperatures for**
348 **different time. Scale bar: 10 μm**
349 **(F) Quantification of the distance of CP29A droplets and nucleoids in (E).**

350 **(G) Subcellular localization of mGFP::CP29Afl or mGFP::CP29AΔPLD at standard growth**
351 **temperatures and after cold acclimation. Two different lines were analyzed for each**
352 **construct (line numbers in white font). Exemplary granules are indicated by arrowheads.**
353 **Scale bar: 2 μm**
354

355 **The PLD is required for plant cold resistance**

356 Null mutants of CP29A show pale tissue at the center of the leaf rosette after longer

357 cold exposure. We next tested whether the PLD is required for CP29A-mediated cold

358 resistance. To this end, we exposed 14 days old plants, expressing

359 mGFP::CP29AΔPLD and mGFP::CP29A in the *cp29a* mutant background, to 8°C for

360 14 days. Additionally, we also exposed 14 days old *cp29a*/SNAP::CP29AΔPLD and

361 *cp29a/*SNAP::CP29A plants to the same cold conditions. The plants expressing full-

362 length CP29A remained green under these conditions, no matter which fluorescent tag

363 was used, demonstrating that the N-terminal fusion protein could functionally replace

364 the wt protein (Figure 4A). By contrast, plants expressing PLD-less protein versions

365 showed a pale center of the rosette, although the affected area appeared smaller than

366 in null mutants and the extent of paleness varied between different individual plants

367 (Figure 4A). This demonstrates that the CP29AΔPLD is not capable of fully reverting

368 the mutant phenotype and only leads to a partial complementation. We conclude that

369 the PLD of CP29A is required for cold-resistance, presumably *via* its ability to phase-
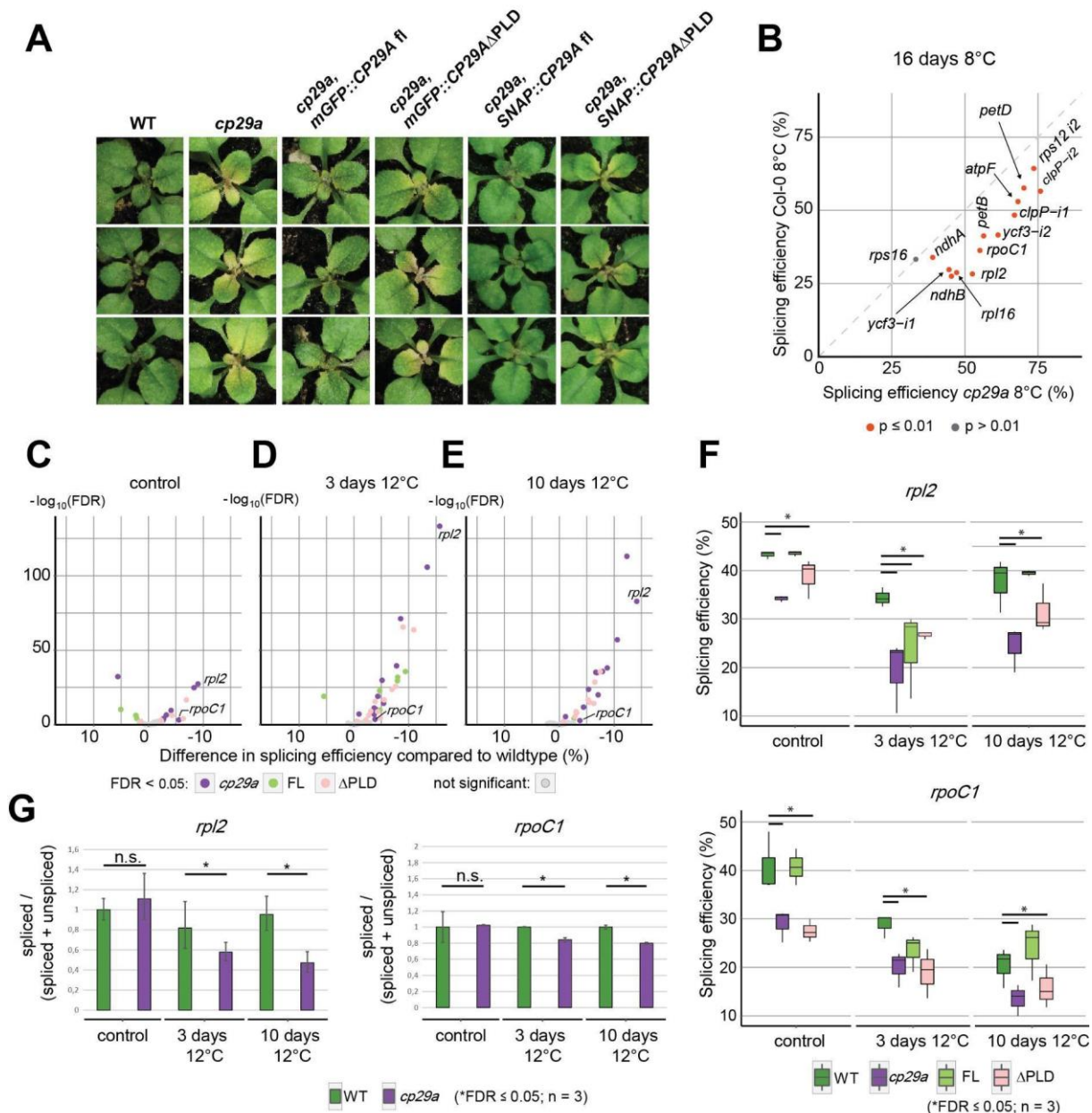
370 separate.

371

Figure 4: Splicing of chloroplast group II introns in the cold depends on CP29A's PLD.

(A) Phenotype of wt, *cp29a* mutants and complementation lines after 14 days at 21°C and 14 days at 8°C.

(B) Analysis of splicing efficiency of chloroplast introns in long-term cold-treated wt and *cp29a* mutant plants by RNA-seq. Splicing efficiency was calculated as the ratio of reads spanning exon-exon junctions versus reads spanning intron-exon boundaries (Castandet et al., 2016).

(C) Analysis of splicing efficiency by RNA-Seq after plant growth for 12 days under standard growth conditions in *cp29a* null mutants, wt and complementation lines. Coloured dots represent introns with significantly changed RNA splicing in the different genotypes (FDR > 5).

(D) Same analysis as in (C) after 12 days at normal temperature and three days of cold treatment at 12°C.

(E) Same analysis as in (C) after 11 days at normal temperature and ten days at 12 °C.

(F) Analysis of RNA-Seq data described in (C-E) specifically for the splicing efficiency of *rpl2* and *rpoC1* mRNAs.

15

(G) Analysis of splicing of *rpl2* and *rpoC1* in wt and *cp29a* mutants after three and ten days at 12°C by qRT-PCR. PCR products were either spanning exon-exon junctions ("spliced") or exon-intron junctions ("unspliced") and splicing efficiency was calculated as the ratio of qPCR-signals of spliced amplicons over the sum of signal for spliced and unspliced amplicons.

Chloroplast RNA splicing defects in long-term cold-treated *cp29a* mutants

To understand the molecular function of CP29A in the cold, we initially sequenced RNA from long-term cold-treated mutant plants and compared it to wt plants to get transcriptome-wide insights into potential gene expression defects. We used young plants, 5 days after germination, since the macroscopic phenotype is restricted to young, emerging tissue. These plants were then kept at 8°C for 16 days, during which time the plants hardly grew. Since the chlorotic, cold-dependent phenotypic defect is present in newly developing leaf tissue only, the non-bleached green cotyledons were removed prior to sampling triplicates. RNA was extracted and ribosomal RNAs were depleted prior to Illumina-based sequencing. A principal component analysis was used to ensure the concordance between replicates and experimental groups (Figure S5A). The comparison of the wt plants grown at low temperatures versus *cp29a* mutant plants grown at low temperatures, showed 661 differentially expressed nuclear genes (DEGs), most of them down-regulated in the mutant (Figure S5B). Among the downregulated genes were many photosynthesis-associated nuclear genes (PhANGs). PhANG expression is specifically downregulated at 21°C versus 8°C in mutants, but not in wt, a case in point being the genes for subunits of the light harvesting complexes (LHCs) and photosystems (Figure S5B,C). This is unsurprising, since defects in chloroplast biogenesis are known to induce the reduction of PhANG expression to avoid wasteful protein production when there are problems with chloroplast development (Richter et al., 2023; Liebers et al., 2022). Or in other words, the effects we observed can be explained by the strong chloroplast developmental phenotype and are thus very likely secondary. We noticed, however, an interesting change in splicing efficiency of chloroplast introns in the RNA-seq dataset. The Arabidopsis chloroplast genome contains 21 introns and we tested their splicing efficiency by comparing reads across exon-exon borders versus reads crossing intron-exon borders (introns in tRNAs could not be assessed because their short exons did not allow the detection of intron-exon spanning reads). We obtained splicing efficiency measurements for 15 introns. With the exception of the intron in *rps16,* which is a pseudogene in Arabidopsis and not spliced (Ueda et al., 2008; Roy et al., 2010),

16

424   splicing was significantly reduced for all introns in cold-treated *cp29a* mutants (Figure
425   4B).

Short-term cold-treated plants do neither display chloroplast development defects nor differential chloroplast RNA accumulation

428   To investigate the onset of molecular defects in the *cp29a* mutant after cold treatment
429   and to avoid measuring secondary effects due to leaf bleaching, we analyzed plants
430   that were exposed to low temperatures for shorter periods. To this end, we harvested
431   tissue that had been grown for 14 days at 21°C and then moved to 8°C for three and
432   ten days, respectively. After three and ten days in the cold, we observed no
433   macroscopic differences between the *cp29a* mutant plants, wt plants and the
434   complementation lines (Figure S6A). To assess the potential occurrence of electron
435   transport problems in the thylakoid membrane after cold treatment, we assayed
436   chlorophyll fluorescence using pulse amplitude modulated fluorescence
437   measurements (PAM). The PAM technique essentially measures changes in PSII
438   photochemical efficiency (in the dark-adapted state), which provides an indicator of
439   electron transport problems in the thylakoid membrane. In long-term treated tissue,
440   *cp29a* mutant plants exhibit a marked increase in fluorescence at the center of the
441   rosette, indicating that normal electron transport in the thylakoid membrane is
442   disturbed (Figure S6B). However, this phenotype is absent in plants exposed to cold
443   for three days, and only a slight increase in fluorescence is measured in *cp29a* plants
444   that were cold-treated for 10 days (Figure S6A).

445   We then harvested the three youngest leaves, extracted total RNA, depleted rRNA,
446   and performed RNA sequencing in biological triplicates. The three biological replicates
447   showed consistent clustering for the different treatments in principal component
448   analysis (PCA), while the four genotypes showed the least differences under control
449   conditions and the most differences after 10 days of cold treatment (Figure S6C). This
450   supports the idea that expression differences between *cp29a* mutants and wt plants
451   occur only in the cold and increase over time. One replicate of the *cp29a* mutant after
452   10 days in the cold and one wt plant after three days in the cold seemed closer to the
453   other replicates. However, it is important to note that a greater difference in biological
454   characteristics between samples can occur due to either uncontrolled environmental
455   factors or inherent variations in plant growth.

17

456   To investigate potential defects in chloroplast gene expression, we compared the wt,

457   mutant, and complemented mutant samples exposed to the same low temperature

458   regime. Firstly, we looked for differences in chloroplast RNA accumulation, but found

459   none in this short-term cold treated material, including mRNAs for components of the

460   photosynthetic machinery (Figure S6D). This is in contrast to long-term cold-treated

461   mutant tissue, where many photosynthesis-related mRNAs are reduced relative to wt

462   (Figure S5). This analysis demonstrated that the secondary, pleiotropic effects

463   observed in long-term cold-treated *cp29a* plants have not yet manifested after short-

464   term cold treatment and that altered chloroplast RNA accumulation is not an early

465   effect in the mutant in the cold.

Splicing in short-term cold-treated tissue depends on CP29A's PLD

467   To investigate splicing defects in short-term cold-treated plants, we analyzed splicing

468   efficiency in our RNA-seq dataset. Even without cold treatment, there were already

469   several introns with significantly reduced splicing efficiencies in the null mutants and

470   ΔPLD plants relative to wt (Figure 4C). No reduction in splicing was observed in the

471   full-length complementation line, but three introns showed increased splicing

472   efficiency. After three days in the cold, the number of introns with significantly reduced

473   splicing efficiency increased in null mutants from seven to twelve and in ΔPLD

474   complementation lines from five to twelve (Figure 4D). Not only did the number of

475   deficiently spliced introns increase, but the strength of their defects also increased in

476   the cold compared to normal temperatures. Unexpectedly, the full-length

477   complementation line exhibited splicing defects after three days in the cold, albeit to a

478   lesser extent than the null mutant and the ΔPLD line. However, these defects

479   disappeared after ten days in the cold, when only one intron showed significantly

480   reduced splicing in full-length complementation lines (Figure 4E). Given that the full-

481   length construct nearly fully complements the null mutation after ten days in the cold,

482   we speculate that the changes in splicing seen at normal temperatures and at three

483   days cold exposure are caused by expression differences of the transgene relative to

484   the endogenous *CP29A* gene. The genomic location of the construct cannot be

485   controlled by the method used, and thus, despite using the same native promoter for

486   all transgenic lines, different expression patterns can occur.

487   The PLD-less version of CP29A, in contrast to the full-length construct, still exhibited

488   pronounced splicing defects after ten days of cold treatment (Figure 4E). The defects

489 were not as strong as in the null mutant, indicating that partial complementation of the

490 splicing defect occurs. These findings were also visualized by comparing splicing

491 efficiency of individual introns. For this, we chose *rpl2,* because it showed the strongest

492 reduction in splicing efficiency in the *cp29a* null mutant (Figure 4D,E). *Rpl2* encodes a

493 subunit of the chloroplast ribosome, which is essential for chloroplast development

494 (Zoschke and Bock, 2018). We also added *rpoC1* to the analysis since its gene product

495 is part of an essential chloroplast gene expression machine, the plastid-encoded RNA

496 polymerase (Hajdukiewicz et al., 1997), and is an example of a gene with a milder

497 splicing deficiency in our RNA-Seq experiment (Figure 4D,E). For both introns, the

498 ΔPLD line can only partially complement the splicing defect of the null mutant (Figure

499 4F). We validated these RNA-seq results by analyzing splicing of *rpl2* and *rpoC1* via

500 qRT-PCR. By amplifying spliced versus unspliced mRNAs, we confirmed the splicing

501 defects of both transcripts in the null mutant (Figure 4G). Overall, our analysis

502 demonstrates that shortcomings in chloroplast splicing are early defects in the *cp29a*

503 mutant after cold exposure and that the PLD is required for full splicing capability in the

504 cold.

Ribosome profiling of *cp29a* mutants suggests a global reduction of chloroplast translation after short-term cold-treatment

507 Given that several introns with reduced splicing are in genes coding for ribosomal

508 proteins, including *rpl2*, we hypothesized that *cp29a* mutants may have translation

509 defects in chloroplasts after cold exposure. We therefore used ribosome profiling

510 (Ribo-seq) in *cp29a* mutants and wt to assess translation. Wt and *cp29a* null mutants

511 were grown for 18 days at 21°C and then shifted to 12°C for three days (in three

512 biological replicates). Like in the RNA-seq assays discussed above, the rationale

513 behind this short and mild cold treatment was that we avoid pleiotropic effects of the

514 bleaching phenotype after long-term cold-treated tissue. Whole leaf tissue was

515 processed for Ribo-Seq analysis as well as for parallel RNA-Seq. Ribosomal RNA was

516 depleted from all libraries. Ribo-seq reads mapping to the chloroplast displayed the

517 previously described broad size distribution(Chotewutmontri and Barkan, 2016),

518 whereas reads mapping to nuclear genes resulted in the expected narrower size

519 distribution for cytosolic ribosomes, peaking at 29 nt (Figure S7A). The footprints

520 mapped predominantly to coding regions, where they show the expected periodicity

521 and preference for the first reading frame, (Figure S7B). The Ribo-seq and RNA-seq

522   RPKM values showed a high level of consistency between the replicates (Figure
523   S7C,D), with each replicate comprising at least 2 million Ribo-seq reads and 4 million
524   RNA-seq reads mapping to the chloroplast transcriptome (Table S2).

525   Standard Ribo-seq and RNA-seq analyses usually rely on detecting a limited number
526   of transcript changes in a large set of transcripts, of which the majority remains
527   unchanged between conditions and genotypes. In a small transcriptome like the
528   chloroplast, a general effect on translation is expected to affect the majority, if not all,
529   of the 80 protein-coding transcripts. Standard normalization of individual sequencing
530   libraries for chloroplast sequencing depth would mask any such general effect. To
531   address this, we compared all chloroplast reads in a sample with all nuclear reads
532   across replicates, thus performing a sample-internal normalization against the nuclear
533   ribosome footprints. This analysis revealed a significant global reduction in chloroplast
534   ribosome footprints in cold-treated mutants versus cold-treated wt (Figure 5A). In
535   contrast, a parallel comparison of the RNA-Seq reads from chloroplasts versus nuclear
536   reads did not show a global change in transcript abundance in the mutant (Figure 5B).
537   This is consistent with our RNA-Seq results from short-term cold-treated mutants and
538   complementation lines: There are no differences in chloroplast RNA accumulation after
539   three and ten days of cold between wt and *cp29a* mutants and there are only a handful
540   of nuclear transcript changes in these libraries (Figure S6D). Similarly, there are no
541   changes in chloroplast transcript abundance and few changes in nuclear transcripts
542   between complementation lines using the full-length CP29A or a PLD-less version of
543   the protein after short-term cold-treated plants (Figure S7D). These results suggest
544   that the reduction in translation observed is not caused by a destabilization of
545   chloroplast transcripts. Therefore, we conclude that translation is globally reduced in
546   *cp29a* cold-treated mutants, likely contributing to the defects in chloroplast biogenesis
547   observed after long-term cold-treatment.

548   Ribosome occupancy can serve as a readout for splicing efficiency in chloroplasts
549   since, unlike in the nucleo-cytosolic compartment, translation and splicing are not
550   separated (Zoschke et al., 2013; Zoschke and Bock, 2018). As a result of a splicing
551   defect, ribosomes accumulate in the first exon but cannot reach the second exon in
552   unspliced chloroplast mRNAs. Thus, the second-to-first exon read ratio is informative
553   for splicing efficiency. We tested this for all chloroplast introns that had at least 50
554   reads per adjacent exon. We found a significant reduction in Ribo-Seq reads for the

20

555   second-exon-over-first-exon ratio for five out of six intron-containing mRNAs in cold-

556   treated mutants compared to wt samples (Figure 5C). In contrast, RNA-seq data show

557   no significant change in RNA coverage between the second and first exon for the same

558   intron-containing genes (Figure 5D). This further supports the requirement of CP29A

559   for efficient splicing of chloroplast introns early after cold treatment. In summary, Ribo-

560   seq reveals that both splicing and translation are reduced in three-day cold-treated
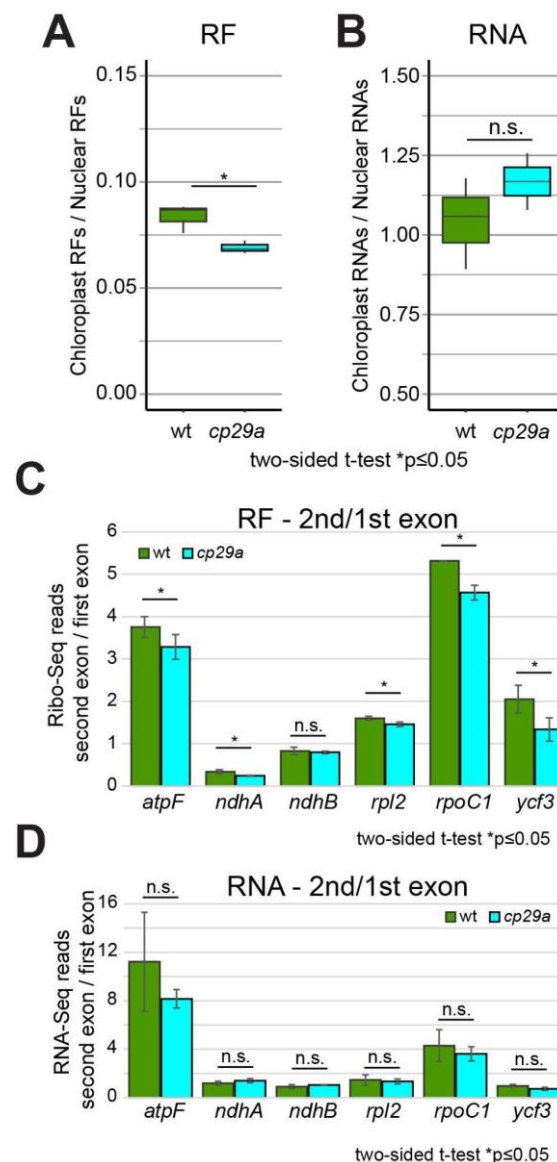
561   mutants.

562

563   **Figure 5: Ribosome profiling and RNA sequencing of short-term cold-treated mutants versus wt.**

564   **A) The ratio of ribosome footprints from chloroplast versus nuclear mRNAs is shown for**

565   **cold-treated (12°C - 3 days) wt and *cp29a* mutant plants. The ratios of three individual**

566   **biological replicates are shown as black dots. Two sided t-tests; *p = 0.001.**

21

567   **B) The ratio of RNA-Seq reads for chloroplast and nuclear mRNAs based on RNA**
568   **preparations from the same batch of plants as in (A).**

569   **C)** **Analysis of splicing efficiency in Ribo-Seq data by calculating the ratio of Ribo-Seq**
570   **reads in the second over the first exon of the chloroplast mRNAs. Two sided t-tests *p**
571   **$\leq$ 0.05.**

572   **D)** **Analysis of splicing efficiency in RNA-Seq data analogous to (C).**

573

Discussion

The PLD of CP29A is required for efficient chloroplast RNA splicing in the cold

576 We have established that the chloroplast RNA binding protein CP29A forms droplet-
577 like structures within chloroplasts, which are more prominent in cold conditions. These
578 droplets rely on the presence of the PLD in CP29A, suggesting that they form through
579 phase separation. This is consistent with what we observe in vitro and based on our
580 NMR analysis of full-length and the PLD-only proteins. Our analyses of *cp29a* mutants
581 and complementation lines have revealed that a first detectable effect after cold
582 exposure is reduced splicing efficiency. Even at normal growth temperatures, we have
583 observed minor but significant splicing issues. While splicing is not completely lost in
584 null mutants and ΔPLD mutants after cold treatment, it is noticeably reduced. Based
585 on our findings, we propose several possible explanations for the splicing defect.

586 Firstly, CP29A may directly act as a splicing factor for chloroplast introns. These introns
587 belong to bacterial group II introns, which require complex 3D structures for proper
588 splicing (Zhao and Pyle, 2017). Previous studies have shown that low temperatures
589 can hinder group II splicing by disrupting the intron's internal interactions (Dong et al.,
590 2020). We suspect that kinetic traps stabilize alternative RNA structures, which are not
591 biologically functional and impede splicing. In bacteria, RNA binding proteins can aid
592 correct RNA folding at low-temperatures (Lindquist and Mertens, 2018), and bacterial
593 intron maturases can rescue splicing of bacterial introns in the cold (Dong et al., 2020).
594 CP29A may fulfill a similar role by directly interacting with the intron and acting as an
595 RNA chaperone. Arabidopsis CP29A has been previously found to associate with most
596 chloroplast mRNAs in RIP-chip experiments (Kupsch et al., 2012), but a preference for
597 introns was not reported. Relatives of CP29A in tobacco showed a preference for
598 unspliced RNAs in co-immunoprecipitation experiments (Nakamura et al., 1999), and

599 were shown to directly bind RNA in vitro (Ye and Sugiura, 1992; Li and Sugiura, 1991).
600 Thus a direct role of CP29A acting as an RNA chaperone cannot be ruled out at
601 present, but our finding that CP29A forms condensates also supports an alternative
602 mechanism.

603 Recent studies provide evidence supporting the functional significance of condensate
604 formation in RNA processing. These studies demonstrate that modifying or eliminating
605 protein domains that facilitate phase separation in RNA-binding proteins (RBPs) can
606 impact mRNA maturation (Wang et al., 2018a; Gueroussov et al., 2017; Ying et al.,
607 2017; Li et al., 2020). This phenomenon has also been observed in splicing. Both
608 RBFOX1 and members of the hnRNP A/D family promote splicing of their target RNAs
609 through condensate formation mediated by intrinsically disordered regions (IDR; Ying
610 et al., 2017; Gueroussov et al., 2017). Similarly, the PLD of the *Arabidopsis thaliana*
611 flowering control locus A (FCA) facilitates the creation of nuclear phase-separated
612 bodies that enhance the polyadenylation of target RNAs (Fang et al., 2019). Phase-
613 separated compartments involved in RNA maturation often exhibit higher
614 concentrations of the associated components compared to the non-condensed phase.
615 Such an increase in the concentration of splicing factors would promote the splicing
616 reaction. Chloroplast introns always depend on sets of splicing factors that have
617 overlapping, but not fully redundant intron specificities (recently reviewed in Lee and
618 Kang, 2020; Wang et al., 2022). Speculatively, these chloroplast RNA splicing factors
619 are recruited to CP29A droplets, thus locally enhancing their concentration in the
620 presence of nascent transcripts from the nucleoid. Future cataloging of the
621 components of the CP29A droplets has the potential to determine whether other known
622 chloroplast splicing factors are enriched in the condensed phase.

Early splicing and translation defects explain impaired chloroplast biogenesis
in cold-treated *cp29a* mutants

625 The first molecular abnormalities observed in *cp29a* mutants after exposure to cold
626 temperatures are a decrease in splicing efficiency and reduced ribosome occupancy
627 of chloroplast mRNAs. These changes occur before any visible effects on
628 photosynthesis and chloroplast development. Conversely, alterations in RNA steady-
629 states in both the chloroplast and nuclear-cytosolic compartments are insignificant. We
630 propose that the splicing and translation impairments are the underlying causes for the

23

631   inability to produce normally green tissue in *cp29a* mutants under long-term cold
632   conditions for the following reasons.

633   Firstly, most of the chloroplast genes containing introns are directly involved in the
634   production of the photosynthetic apparatus or encode essential components of the
635   chloroplast gene expression machinery (de Longevialle et al., 2010; Small et al., 2023).
636   For example, the proteins encoded by intron-containing genes *atpF* and *petB/petD* are
637   vital components of the chloroplast ATP synthase and the cytochrome b_6f complex,
638   respectively (Kroeger et al., 2009; Till et al., 2001). Knocking out any of these three
639   genes results in the loss of photosynthesis, leading to pale tissue (Schwenkert et al.,
640   2007) and the absence of splicing in *atpF* alone leads to pale plants and seedling death
641   (Till et al., 2001). Therefore, a reduction in splicing efficiency for *atpF* and *petB/petD* is
642   expected to strain the assembly of the photosynthetic machinery, which becomes
643   critical in cold temperatures where photosystem assembly is expected to be slower.

644   In addition to the direct impact on photosynthesis gene expression, cold-treated *cp29a*
645   mutants are expected to face general difficulties in producing the chloroplast gene
646   expression machinery, particularly the ribosome. We identified three chloroplast
647   mRNAs encoding ribosomal proteins L2, S12, L16 that show reduced splicing
648   efficiency. Among them, *rpl2* exhibits the most significant splicing defect in our dataset.
649   Therefore, the most plausible explanation for the observed translation defect in cold-
650   treated *cp29a* mutants is the reduced splicing deficiencies of these three mRNAs and
651   thus a limitation in ribosome production. It is however important to acknowledge that
652   we cannot rule out a more direct role of CP29A in chloroplast translation at this stage.
653   The central question remains: How does the reduced translation contribute to the
654   failure to generate green tissue in cold-treated *cp29a* mutants? Loss of the chloroplast
655   ribosome is embryonic lethal in *Arabidopsis thaliana* (Zoschke and Bock, 2018), and
656   hypomorphic mutations in ribosomal protein genes result in the loss of photosynthesis
657   (Dupouy et al., 2022; Bobik et al., 2019). Therefore, the general reduction in chloroplast
658   translation in cold-treated *cp29a* mutants is expected to contribute to the inability to
659   produce photosynthetic tissue. In bacteria, the production and maintenance of
660   ribosomes themselves require specific proteins induced at low temperatures (Jones et
661   al., 1996; Dammel and Noller, 1995), and de novo assembly of newly synthesized
662   bacterial ribosomes is stimulated during cold shock (Charollais et al., 2004).
663   Interestingly, many mutants affecting chloroplast translation exhibit bleaching

24

664 phenotypes induced by low temperatures, suggesting that any impairment of
665 chloroplast translation will compromise chloroplast development and thus the
666 production of green tissue (Kusumi et al., 2011; Liu et al., 2010; Gao et al., 2022). In
667 fact, a general decrease in translation caused by splicing defects in ribosomal protein
668 mRNAs will also impact the production of chloroplast ribosomes themselves,
669 amplifying the defect. Together, deficiencies in chloroplast translation are likely at the
670 very least contributing to, if not decisively causing, the failure of chloroplast
671 development in *cp29a* mutants in cold conditions.

672 **Nucleoids as neighbors of a chloroplast RNA processing compartment**

673 Chloroplast DNA is structured into nucleoids, which consist of multiple chromosomes
674 and associated proteins. Our study reveals that the droplets formed by CP29A are
675 primarily found in close proximity to nucleoids. This observation bears similarity to the
676 formation of RNA droplets in the mitochondria of metazoans, which are also spatially
677 associated with nucleoids (Jourdain et al., 2016; Antonicka et al., 2013). The
678 localization of CP29A droplets near nucleoids suggests a potential functional
679 connection between these two cellular components. Just as RNA granules in
680 mitochondria are believed to play a role in RNA regulation and processing, the
681 proximity of CP29A granules to nucleoids implies a similar involvement in chloroplast
682 RNA-related processes. Nucleoid-associated mitochondrial granules contain newly
683 synthesized mitochondrial RNA and contain various RNA binding proteins and RNases
684 required for RNA maturation (Borowski et al., 2012; Pearce et al., 2017). Currently, the
685 composition of CP29A-containing droplets remains unclear, and its protein interaction
686 partners are unknown. Interestingly, a fraction enriched with nucleoids from maize
687 contained factors involved in mRNA processing, splicing, and editing, including
688 homologs of CP29A (Majeran et al., 2011). This led to the suggestion that RNA
689 processing occurs co-transcriptionally. Our identification of a droplet structure adjacent
690 to nucleoids suggests that further subcompartmentalization of gene expression takes
691 place in chloroplasts, separate from nucleoids. The observed distance of 200-240 nm
692 between nucleoids and CP29A droplets implies the possibility of an RNA bridge formed
693 by nascent transcripts (considering that a 1000-nucleotide (nt) RNA molecule is
694 approximately 300 nm in length). This proximity suggests that nascent transcripts could
695 directly interact with CP29A droplets, facilitating RNA processing and other related
696 molecular events. While splicing may be one function of such granular structures, it

25

697   remains an exciting question for future studies whether other RNA processing steps
698   occur here or in additional separate compartments. The existence of PLDs in a large
699   number of plant proteins suggests that we can anticipate the discovery of many more
700   phase condensation events, including those occurring within organelles (Chakrabortee
701   et al., 2016).

CP29A droplets as a compartment for cold acclimation

703   In metazoans, phase separation processes are used as temperature sensors in
704   various contexts (Li and Fang, 2020). Plants, as sessile organisms, need mechanisms
705   to acclimate to changing temperatures. However, examples of temperature-dependent
706   phase separation in plants are rare. In Arabidopsis, increased temperature leads to
707   PLD-mediated phase separation of EARLY FLOWERING 3 (ELF3), which regulates
708   the circadian clock (Jung et al., 2020). Another example is GUANYLATE BINDING
709   PROTEIN LIKE 3 (GBPL3), which undergoes phase separation through a C-terminal
710   IDR, resulting in the activation of target promoters during pathogen infection - a
711   process impaired at higher temperatures (Huang et al., 2021a). Similarly, higher
712   temperatures lead to the dissolution of phase separation-dependent, phytochrome-
713   containing photobodies, thereby modulating light-responsive gene expression (Chen
714   et al., 2022). CP29A differs from these phase separation events in terms of its specific
715   occurrence and importance at low temperatures. Its ability to autonomously and rapidly
716   form condensates in response to lower temperatures in vitro and to occur in granular
717   structures upon cold exposure in vivo together with its cold-specific function in
718   chloroplast development make it a possible chloroplast cold sensor.

719   At first glance, CP29A droplets appear similar to cytosolic stress granules in mammals
720   and yeast, which can be induced by low temperatures (Hofmann et al., 2012).
721   However, stress granules mostly repress translation and may eventually contribute to
722   RNA degradation (Hofmann et al., 2012). In contrast, CP29A droplets seem to support
723   the accumulation of spliced transcripts and facilitate translation. We interpret CP29A
724   as a factor that helps maintain the chloroplast gene expression program under low-
725   temperature conditions, while stress granules aid in terminating a gene expression
726   program, paving the way for preparing an alternative program to counter the stress
727   (Ivanov et al., 2019). It should be noted that the temperatures used to induce stress
728   granules in mammals are considered well outside the regular physiological range that
729   occurs in mammalian tissues (Lowering from 37° to 10°; Hofmann et al., 2012), while

730 CP29A becomes relevant during mild temperature changes (21°C to 12°C) that
731 frequently occur throughout the seasons in plant leaves. Thus, cold-dependent phase
732 separation of CP29 occurs at relevant temperatures where the ability to sense and
733 react to dropping temperatures is permanently needed.

734 Another interesting difference of CP29A phase separation compared to other thermo-
735 sensitive phase separation events may lie in the mechanism of droplet formation.
736 Several other RNA-binding proteins that exhibit temperature-dependent phase
737 separation, such as Fused in Sarcoma (FUS), heterogeneous nuclear
738 ribonucleoprotein A1 (hnRNPA1), or the poly(A)-binding Protein1 (Pab1), utilize their
739 RNA-binding domains next to their IDRs to drive phase separation (Molliex et al., 2015;
740 Burke et al., 2015; Yoshizawa et al., 2018; Riback et al., 2017). For example, in the
741 case of FUS, phase separation is supported by the cold denaturation of its zinc finger
742 domain (Félix et al., 2023). Our in vitro and in vivo deletion analyses suggest that for
743 CP29A, the PLD is the dominant factor in mediating cold-induced phase separation.
744 We hypothesize that the RRMs remain intact and uninvolved during phase separation
745 and fulfill important roles inside the droplet, likely in RNA binding. The fact that the
746 PLD-less version of CP29A was still able to partially complement the macroscopic and
747 splicing phenotype of the null mutant in the cold supports this idea. Identifying CP29A's
748 RNA and protein partners within the droplet will be a crucial next step in understanding
749 the exact mechanism of its effects on splicing and translation. CP29A has been
750 identified in a proteome of heat-induced chloroplast stress granules together with other
751 RNA binding proteins, including chloroplast RNA splicing and RNA editing factors
752 (Chodasiewicz et al., 2020). These granules were induced by treating Arabidopsis
753 seedlings for 30' min at 42°C, conditions that led to irreversible aggregation of
754 recombinant CP29A in our hands. Targeted proteomic analyses will have to show
755 whether the cold-induced CP29A granules are related to these heat induced stress
756 granules in protein composition and function.

757 The biochemical and biophysical conditions within chloroplasts with its light-induced
758 changes in pH and redox state are in many aspects different from the nucleo-cytosolic
759 compartment. Oxidative stress has been shown to induce stress granules in
760 chloroplasts from the green algae *C. reinhardtii,* the only other case of a granule
761 affecting gene expression in chloroplasts (Uniacke and Zerges, 2008). Orthologs of
762 cpRNPs are missing in green algae (Ruwe et al., 2011) and stress granules in *C.*

27

763   *reinhardtii* are likely functionally and mechanistically quite different from CP29A-

764   droplets. In order to explore the role of CP29A in temperature acclimation it is probably

765   more promising to tap the diversity of Arabidopsis accessions to uncover whether

766   sequence changes in the PLD modulate its ability to phase separate and thus act as

767   part of a thermosensitive response for different temperature ranges.

768

Acknowledgements

Author Contributions

782   C.S. and M.S. conceived the study, designed the strategy and supervised the

783   experiments. J.L., B.L., N.K. S.G. and Y.G. performed the experiments and interpreted

784   the data. S.M., W.W., E.K and R.Z. analyzed datasets and interpreted data. C.S. wrote

785   the manuscript, which was edited by all co-authors.

Declaration of Interests

787   The authors declare no competing interests.

788

Material and Methods

Bacterial Strains and growth

791   DH5α *E. coli* (Invitrogen-Thermo Fisher, Hennigsdorf, Germany) was used for vector

792   amplification and passing, while BL21 *E. coli* (Invitrogen-Thermo Fisher, Hennigsdorf,

793   Germany) was used for protein expression. *E. coli* cultures were grown at 37C under

794 constant shaking (180 rpm) in standard lysogeny broth (LB) medium. *Agrobacterium*
795 *tumefaciens* GC3103 cultures were grown at 28°C under constant shaking (200 rpm)
796 in standard lysogeny broth (LB) medium.

Plant lines

798 Null mutants of *CP29A* (*cp29a-6*) were obtained from the SALK Institute (San Diego)
799 and were previously described (Kupsch et al., 2012). For transformation, the *cp29a-6*
800 line was grown under standard conditions (long day conditions; 120 µE s^{-1}m^{-2}) in a
801 growth chamber. *Agrobacterium* mediated transformation was carried out by standard
802 floral dip methods.

Plant growth conditions

804 Arabidopsis seeds were stratified at 4°C in the dark for 3 days and then grown at 21°C
805 with a light intensity of 120 µmol m^{-2}s^{-1}. For short-term cold treatment, plants were
806 grown for 14 days at 21°C and then transferred to 12°C or 8°C for 3 or 10 days. To
807 analyze the effects of long-term cold stress on *cp29a* and wt plants, both sets of plants
808 needed to be at the same developmental stage. Due to slower growth under cold
809 stress, cold-stressed plants were cultivated for 21 days to reach a comparable
810 developmental stage as unstressed plants grown for 10 days at 21°C. This involved
811 an initial cultivation at 21°C for 5 days, followed by an additional 16 days at 8°C. Before
812 harvesting, cotyledons were removed since the phenotypic effect of a *CP29A* knockout
813 under cold conditions is primarily observed in newly formed tissues.

Construction of plant transformation vectors and plant transformation

815 Transformation vectors for the preparation of plant transgenic lines carrying mGFP and
816 SNAP Tags were generated by HiFi assembly. The promoter region of CP29A was
817 amplified with the primer pair pcp29A+70aa_frw and pcp29A+SP70aa_rev, resulting
818 in a 1454 bp fragment (All oligonucleotides used for cloning can be found in Table S3).
819 A monomeric GFP fragment was obtained using the primer pair mGFP FL CP29A_frw
820 and mGFP FL CP29A_rev, yielding a 722 bp fragment. The full-length genomic
821 sequence of CP29A was amplified with the primer pair CP29A genomic+3UTR_frw
822 and CP29A genomic+3UTR_rev, resulting in a 2234 bp fragment. These three
823 fragments were mixed in equimolar concentration with the pGL1 Vector cut with *Bam*HI
824 and *Hind*III. HiFi Assembly was performed following the manufacturer's protocol (NEB,
825 Frankfurt, Germany), resulting in the generation of a vector named pGL1-
826 pcp29A::mGFP::CP29AFL.

827 For an analogous SNAP-tagged version of the full-length protein, the promoter region,
828 SNAP Tag, and genomic fragment of CP29A were amplified with the following primer
829 pairs: pcp29a+70aa_frw and pcp29A+70aa_rev for the promoter region, SNAptag_frw
830 and SNAPtag_rev for the SNAP Tag, and CP29AFL SNAPtag_frw and CP29AFL
831 SNAPTag_rev for the genomic fragment. The size of the SNAP Tag fragment was 579
832 bp, while the sizes of the other fragments were as described above for the GFP
833 construct. After HiFi assembly into pGL1, the vector was named pGL1-
834 pcp29A::SNAP::CP29AFL.

835 To obtain a version of the constructs without the PLD domain, additional primer pairs
836 were used. The promoter region and the GFP tag were amplified using the same primer
837 pairs as before. A first genomic CP29A fragment, encompassing the RRM1 region,
838 was amplified with the primer pair CP29Amidpart-PLD_frw and CP29Amidpart-

839 PLD_rev, resulting in a 927 bp fragment. The second part of the genomic CP29A
840 sequence, excluding the PLD domain, was amplified with the primer pair CP29ACterm-
841 PLD_frw and CP29ACterm-PLD_rev, resulting in a 1230 bp fragment. After combining
842 these PCR fragments with the pGL1 Vector, a HiFi assembly reaction was performed,
843 resulting in the generation of a vector named pGL1-pcp29A::mGFP::CP29A DPLD.

844 After confirming the sequence of the PLD-less mGFP-tagged construct through Sanger
845 sequencing, the primer pair for the full-length SNAP Tag construct was used on the
846 template of a GFP construct lacking the PLD domain. This allowed for the generation
847 of a SNAP Tag version of the construct without the PLD domain, resulting in a PCR
848 fragment of 2139 bp. The resulting vector was named pGL1-pcp29A::SNAP::CP29A
849 DPLD.   Primer   design   was   performed   using   NEBuilder   v2.8.1
850 (https://nebuilder.neb.com/#!/).

851 Bacteria carrying all fragments in the pGL1 Vector derivatives were selected on LB
852 media supplemented with Kanamycin. Transgenic plants generated by Agrobacterium
853 mediated transformation were selected on soil by spraying with BASTA. At least three
854 independent lines per construct were isolated.

855 **Photosynthetic measurements**

856 In vivo chlorophyll a fluorescence was monitored with the Imaging PAM chlorophyll
857 fluorimeter (Imaging PAM, M-Series; Walz, Effeltrich, Germany). Plants were dark-
858 adapted for 15 min and measured according to standard protocols (Klughammer and
859 Schreiber, 2008).

860 **Construction of Bacterial Expression Vectors**

861 Vectors for the expression of the CP29A protein in *E. coli* were prepared using the HiFi
862 Assembly protocol with primer-based cloning. To amplify the full-length version of the
863 CP29A protein, the primer pair Nitin_RRM1+2ext(wt)fw and Nitin_RRM1+2ext(wt)rev
864 was used, resulting in a 837 bp fragment. This fragment was assembled into the
865 pETM11 vector backbone, which had been cut with *Nco*I and *Bam*HI, generating a
866 vector named pETM11-CP29A FL.

867 Similar protocols were followed for the preparation of constructs for NMR
868 measurements. For the construct carrying only the first RRM1 domain, the primer pair
869 FR09 and FR10 was used, resulting in a 321 bp fragment. The fragment carrying the
870 RRM2 domain was amplified using the primer pair FR11 and FR12, also resulting in a
871 321 bp fragment. Each of these fragments was inserted into the pETM11 vector, which
872 had been cut with *Nco*I and *Bam*HI, using HiFi Assembly.

873 For cloning of the PLD-only domain, the primer pair Nitin_PLD_fw and Nitin_PLD_rev
874 was used, resulting in a fragment of an unspecified size. This fragment was cloned into
875 the pTrx Vector backbone, which had been cut with *Nco*I and *Bam*HI, and processed
876 with the HiFi Assembly Kit (NEB, Frankfurt, Germany). The resulting vector was named
877 pTrx-CP29APLD core.

878 For droplet formation assays, constructs were prepared in the pETM11 vector
879 backbone. These constructs contained the mNeon Green Tag fused to the N-terminal
880 side of the CP29A protein. The CP29A full-length version was amplified using the
881 primer pair pETM11 mNeonGreen frw and mNeonGreen29Arev which resulted in a
882 PCR fragment size of 956bp. The mNeonGreen Tag was amplified separately using

883 the primer pair mNeonGreen29A_frw and pETM11 29A_rev which resulted in the
884 fragment size of 753bp. The combination of these PCR products with the NcoI and
885 BamHI-digested pETM11 vector produced the pETM11-mNG::CP29AFL expression
886 vector.

887 The PLD domain fused to the mNeon Green Tag was amplified using the primer pairs
888 pETM11-mNeonGreen_frw and mNeonGreen_PLD_cor_rev and the PCR product
889 obtained was of 753bp in size, as well as mNeonGreen PLD_cor_frw and
890 pETM11_PLD_cor_rev which amplified a PCR product of 264 bp in size. The resulting
891 fragments were used for HiFi assembly to generate the pETM11-mNG::PLDcore
892 vector.

893 **Protoplast Isolation and Microscopy**

894 For protoplast isolation, plants were grown on soil for 14 days at standard growth
895 conditions and used for protoplast isolation (Yoo et al., 2007). 10^6 protoplasts were
896 used for in vivo labeling. SNAP-tagged proteins were labelled with Cell-SiR647 (NEB,
897 Frankfurt, Germany). Labeling was done at RT for 1hr, according to the manufacturer's
898 protocol. After labeling, a wash step with MMG Buffer was included before fixation.
899 Protoplasts were fixed in ice cold 4% paraformaldehyde in the PBS buffer pH7.2 for 15
900 minutes. After fixation, three wash steps with ice cold methanol were used for
901 chlorophyll extraction. After a PBS wash, DAPI staining (50 ng/ml) was done in PBS
902 buffer at RT for 30 min. The DAPI stain was washed off 5 times with PBS Buffer. Slides
903 with fixed protoplasts were analyzed using different microscopes. Fig. 3A: Abberior
904 Facility Line Confocal Microscope (Aberrior GmbH, Göttingen, Germany). Fig. 3B:
905 Protoplasts were mounted in Prolong Mountant (Invitrogen, Hennigsdorf, Germany) for
906 STED Microscopy on a Leica TCS SP8 3X (Leica, Wetzlar, Germany). A deconvoluted
907 image of the STED scan is shown, performed with Leica Las X & Huygens
908 Deconvolution software. Fig. 3E: Protoplasts were mounted in Mowiol (Fang et al.,
909 2019) for STED and confocal imaging using the STED Abberior Facility Line machine
910 (Abberior, Göttingen, Germany) and a 100x oil-immersion objective. The DAPI signal
911 of nucleoids was excited with a 405 nm laser, and the emitted light was collected with
912 a detector in the range of 415 to 525 nm. The SNAP Cell SiR647 dye was excited with
913 a 640 nm laser in confocal or STED mode, and the emitted light was collected within
914 the range of 650 to 735 nm for autofluorescence of chlorophyll and fluorescence of
915 SiR647, respectively. SNAP dye-labeled droplets were detected by STED microscropy
916 using excitation at 640 nm and a detecting spectrum of 650 to 735 nm, while the STED
917 laser emitting light used here was at 775 nm with a gate of 750 ps (+8 ns). Fig. 3G:
918 Confocal images from live cell imaging of plant tissue grown at room temperature and
919 plants exposed to cold conditions for 3 days at 12°C. Simultaneous images were taken
920 in the eGFP and STAR635 channels in order to detect eGFP and chlorophyll
921 autofluorescence. Excitation of EGFP was performed with a laser at 518 nm, and the
922 emitted light was collected in the range of 520 to 550 nm, while the STAR635 signal
923 was excited with a laser at 640 nm, and the emitted light was collected within the range
924 of 645 to 670 nm.

925

926 **Immunofluorescence assay of CP29A droplets in protoplasts**

927 Protoplasts were allowed to adhere for 10 minutes at room temperature on poly-L-
928 lysine-coated slides. The protoplasts were then fixed with 4% formaldehyde (w/v) in
929 PBS (137 mM NaCl, 2,7 mM KCl, 10 mM Na2HPO4, 2 mM KH2PO4) for 20 minutes

930 at room temperature. To extract chlorophyll, the cells were incubated for 2 x 10 minutes
931 at -20 °C in pre-cooled methanol. Afterwards, the fixed cells were washed for 2 x 10
932 minutes in PBS-Mg (5 mM MgCl$_2$ in PBS). Permeabilization was carried out at room
933 temperature for 10 minutes in 2% Triton or 4% DMSO in PBS. The protoplasts were
934 then equilibrated for 2 x 10 minutes in PBS-Mg and subsequently used for
935 immunofluorescence staining.

936 The fixed protoplasts were blocked for 30 minutes at room temperature in 0.5% (v/v)
937 BSA in PBS, pH 7.2. The cells were incubated for 75 minutes at 37°C with 2% Triton
938 in PBS for 10 minutes at RT to improve penetration of the antibody. The cells were
939 then incubated with the primary antibody against CP29A(Kupsch et al., 2012; diluted
940 in 0.5% (v/v) BSA in PBS); diluted in 0.5% (v/v) BSA in PBS (dilutions of 1:50 or 1:500
941 were used). After washing twice for 10 minutes in PBS-Mg, the cells were incubated
942 with a fluorescein-labeled secondary antibody (diluted in 0.5% (v/v) BSA in PBS) for
943 45 minutes at room temperature in the dark. The samples were then equilibrated again
944 for 2 x 10 minutes in PBS-Mg. Finally, a drop of the permanent mountant
945 VECTASHIELD® HardSetTM Antifade Mounting Medium (Life Technologies,
946 Carlsbad) was added to cover the cells. To preserve the preparation, the specimen
947 was sealed with nail polish.

948 Epifluorescence microscopy of immunofluorescence assays was carried out with a
949 IX71 ΔVision Spectris Restorations microscopy system (Olympus, Tokyo), employing
950 the 100x Plan Apo objective (numerical aperture 1.4).

951 **Protein expression and purification**

952 mNG::CP29AFL, mNG::CP29A ΔPLD, and mNG::PLD were expressed in *E. coli* BL21
953 at 18°C overnight after induction with 0.1 mM Isopropyl β-D-1-thiogalactopyranoside.
954 Bacterial pellets were resuspended in a resuspension buffer (20mM Na-Phosphate
955 Buffer pH 7.4, 300mM NaCl and 1mg/ml Lysozyme). Cells were lysed by sonication
956 and the lysate was centrifuged at 12,000 g for 15 minutes at 4°C. Supernatants were
957 incubated with pre-washed agarose Ni-NTA beads (Cytiva, Freiburg). Bound protein
958 was washed five times with 5 volumes of the bead bed with increasing NaCl
959 concentration (Wash Buffer 1:10mM Tris pH8, 300mMNaCl + 5mM imidazole; Wash
960 Buffer 2: 10mM Tris pH8, 500mM NaCl + 5mM imidazole; Wash Buffer 3:10mM Tris
961 pH8, 1000mMNaCl; Wash Buffer 4: 10mM Tris pH8, 1500mM NaCl). Before elution, a
962 TEV cleavage step was performed with addition of 1000 U of the enzyme per ml of the
963 suspension. Elution of the bound protein was done in 3 Volumes of the bead bed (150
964 mM NaCl, 10 mM Tris pH 8, 300 mM Imidazole, 1 mM DTT, 0.5mM EDTA). Eluate was
965 concentrated using centricon tubes (Merck, Darmstadt). Protein concentrations were
966 estimated via Bradford assays using a BSA standard. Protein purity was estimated via
967 PAGE-SDS and subsequent CBB staining of the gel.

968 **In vitro phase separation assays**

969 In vitro phase separation assays with purified recombinant protein were performed in
970 low salt buffer (10mM Tris pH8.0, 50mM NaCl, 1mM DTT, 0,5mM EDTA, 2,5%
971 Glycerol). Crowding agent was added to 10% as a final concentration through mixing
972 with the microscopy solution (20% PEG 8000 in low salt buffer). After mixing, the
973 sample was applied to an 8 well glass bottom slide (Ibidi), incubated at room
974 temperature for 30 seconds before being imaged on an Abberior Facility line
975 Microscope with Light Box software using 100x oil magnification objective. Droplet
976 formation was followed over time by collecting a series of images using a 488 nm

977 excitation laser (3% power). All droplet assays were repeated at least three times. For
978 cold treatment, the protein solution was incubated on ice for 10 minutes prior to
979 microscopy. ImageJ software was used for all image processing

980 Quantifications of droplet size were done with a custom python script in ImageJ. After
981 smoothing and background subtraction using a rolling ball algorithm, droplets were
982 detected with the "Analyze Particles" plugin. The measured Feret's diameter -
983 maximum diameter of a round object - was then plotted using R-Studio for different
984 conditions.

985 **Fluorescence recovery after photobleaching**

986 For fluorescence recovery of photobleaching (FRAP) recordings, droplets observed in
987 vitro were excited with 488 nm laser line on confocal Abberior Facility line microscope
988 by using a 100x oil objective. A region of interest was selected within the condensate
989 and 100% power of STED laser was used for bleaching. Five images were taken prior
990 to bleaching and post-bleaching recovery of fluorescence was recorded for up to 55
991 sec at a frame interval of 1 sec. Evaluation of the FRAP analysis was done with help
992 of ImageJ and custom written Python scripts. In brief, for each condition at least 13
993 trajectories were analysed, resulting in the fluorescence intensity within the bleached
994 region. First, trajectories were averaged, calculating the standard deviation
995 represented as shadow for each condition in Fig. 1H. Fluorescence intensity recovery
996 trajectories were then fitted using custom written Python scripts with the formula:

997
$$I(t) = A \cdot (1 - exp(-t/\tau)),$$

998 where A corresponds to the plateau intensity and represents the mobile fraction of
999 proteins, τ the recovery time constant and the time after the bleach pulse. Imaging
1000 and bleaching conditions such as Laser intensity, bleaching geometry and time were
1001 strictly kept constant in between conditions in order to compare mobile fraction and
1002 recovery half time (McSwiggen et al., 2019). The value of τ is extracted and is used to
1003 calculate the recovery half time t ½:

1004
$$t1/2 = \tau \ln(2)$$

1005 **Distance measurements between CP29A droplets and nucleoids**

1006 The shortest distance for every CP29A droplet is measured to its closest nucleoid
1007 based on STED microscopy images with an approx. resolution of 60 nm using an
1008 Aberior instrument. ImageJ was then used to perform peak detection in both channels.
1009 A custom written python script was further used to calculate minimal distances between
1010 CP29A and nucleoid pairs. The minimal distances were plotted as a histogram and
1011 fitted with a kernel density estimation (KDE). At least 5 field of views containing a
1012 minimum of 20 chloroplasts each were analyzed per condition. To confirm the
1013 performance of this experiment, we calculated the number of CP29A droplets and
1014 nucleoids per chloroplast volume and used a custom written python script to randomly
1015 position them. The same script was then used to measure distances. A normalized
1016 probability density function to estimate the average distance between centers resulted
1017 in a mean of 0.46 um.

1018 **NMR spectroscopy**

1019 N-terminal His$_6$-tagged RRM1 (97-176 aa), RRM2 (255-334 aa), RRM1,2 (97-334 aa)
1020 and His$_6$-thioredoxin tagged PLD (176-254 aa) constructs were over-expressed in *E.*
1021 *coli* BL21 (DE3) in M9 minimal media supplemented with ^{15}N NH$_4$Cl and/or ^{13}C glucose
1022 as the sole nitrogen and carbon sources, respectively. Cells were harvested, lysed by
1023 French press and respective proteins were purified by affinity chromatography with Ni-
1024 NTA sepharose followed by TEV cleavage as mentioned above. Further purification
1025 steps were carried out by ion -exchange and size-exclusion chromatography. The final
1026 buffer for NMR samples contained 20 mM sodium phosphate (pH 6.8), 50 mM NaCl, 1
1027 mM DTT. The sample quality was checked by SDS-PAGE and ESI-mass
1028 spectrometry.

1029 Backbone and side-chain chemical shifts for RRM1, PLD and RRM2 constructs of
1030 CP29A were assigned from conventional 3D NMR experiments, such as HNCACB,
1031 CBCA(CO)NH, HNCO, HN(CA)CO, HNN, (H)CCCONH, H(CCCO)NH and ^{15}N-edited
1032 NOESY-HSQC (Sattler, 1999; Panchal et al., 2001). NMR measurements were
1033 performed on Bruker spectrometers with a proton Larmor frequency of 500, 600, 800,
1034 900, 950 or 1200 MHz equipped with cryogenic or room temperature ^{1}H, ^{13}C and ^{15}N
1035 triple resonance probes detection. 5% D$_2$O was added to the samples to lock the
1036 external magnetic field, NMR samples were put into 3 mm, 5 mm or Shigemi tubes.
1037 ^{1}H, ^{15}N HSQC spectra were acquired with 100 ms and 60 ms acquisition time in direct
1038 and indirect dimensions, respectively. Spectra were processed with Bruker Topspin
1039 3.5pl6 or NMRPipe (Delaglio et al., 1995) with a shifted sine-bell window function and
1040 zero filling before Fourier transformation. Proton chemical shifts were referenced
1041 against sodium 2,2-dimethyl-2-silapentane 5-sulfonate (DSS). Spectra were analyzed
1042 by the CCPN (v2.5) software tool (Vranken et al., 2005). Steady-state {^{1}H-}-^{15}N
1043 heteronuclear NOE experiments wererecorded with 170 and 168 ms acquisition times
1044 in the direct and indirect dimension, respectively with 3s recycle delay and 32 scans.
1045 Spectra were split with a Bruker AU-program, further processed in Topspin and then
1046 analyzed using CCPN.

1047 Secondary structural elements for RRM1, PLD and RRM2 domains were derived from
1048 NMR backbone and side-chain chemical shifts using TALOS-N (Farrow et al., 1994)
1049 and compared with an AlphaFold2 model. The structural model of RRM1-PLD-RRM2
1050 was generated using CNS (v1.2; Shen and Bax, 2013) by keeping the ternary fold of
1051 both RRMs (obtained from AlphaFold2), while the coordinates for the PLD linker were
1052 randomized. The electrostatic surface charges for CP29a were calculated by APBS
1053 tool (Baker et al., 2001).

1054 **Small-angle X-ray scattering (SAXS) measurements**

1055 SAXS experiments were carried out in-house on a Rigaku BIOSAXS1000 instrument
1056 comprising a a Rigaku HF007 microfocus rotational anode with a copper target (40 kV,
1057 30 mA). Transmissions were measured with a photodiode beam stop and calibration
1058 was done with a silver behenate sample (Alpha Aeser). All samples were dialyzed
1059 overnight with SAXS buffer (20 mM sodium-phosphate, pH 6.5, 30mM NaCl) before
1060 the measurements. Samples with concentrations from 4 to 16 mg/ml were measured
1061 at 25ºC and 4ºC temperature to assess concentration dependent effects. Multiple
1062 buffer samples were measured in-between each run and buffer subtraction was
1063 applied using the SAXSLab software. Further data analysis was done using the ATSAS
1064 package (v3.0.5; Manalastas-Cantos et al., 2021).

1065 **Immunoblots**

Equal amounts of total leaf protein were separated on an SDS PAGE gel and blotted to nitrocellulose membrane (Cytiva, Freiburg, Germany). Membranes were blocked in 4% milk TBST solution for 1 hour, washed twice with TBST solution and incubated with a GFP-mouse antisera (Invitrogen, Hennigsdorf, Germany), a CP29A specific rabbit antisera (Kupsch et al., 2012) or anti-SNAP rabbit antisear (NEB, Frankfurt, Germany) in 1:2000 dilution overnight at 4°C and subsequently washed with TBST buffer four times at room temperature. Secondary antibodies (either anti-mouse IgG or anti-rabbit IgG, both conjugated to HRP) were used at a dilution of 1:10.000 for GFP/CP29A primary antisera or at 1:5000 for the SNAP primary antisera and incubated for 1 hour at room temperature. Four washes with TBST buffer were done prior chemiluminescent detection.

RNA isolation and library construction for RNA-seq

Plant tissue was frozen in liquid nitrogen and pulverized in a mortar. Total RNA was isolated by acid guanidinium thiocyanate-phenol-chloroform-based extraction and purified from the aqueous phase using the Monarch RNA Clean Up Kit (NEB, Frankfurt, Germany). RNA quality was assessed by agarose gel electrophoresis. Total RNA was sequenced on an Illumina platform using Novogene's (London) lncRNA-seq protocol, based on rRNA-depletion followed by strand-specific library construction. All libraries were sequenced with 150 bp paired-end reads.

RNA-seq - gene expression analysis

The nf-core/rnaseq (v3.10.1) pipeline was used for quality control, read processing and mapping of the RNA-seq libraries. The Hisat2 was used as aligner and TAIR10 and Araport11 were provided to the pipeline as reference genome and annotation, respectively. FeatureCounts (Rsubread, 2.12.0) was used for read counting and DeSeq2 was used for differential gene expression analysis after low read filtering (CPM>1 in all samples).

RNA-seq - splicing analysis

Splicing efficiencies were analyzed using the ChloroSeq pipeline, as described previously (Castandet et al., 2016). Fisher's exact test in combination with Benjamini-Hochberg correction was used for statistical testing.

qPCR

For qPCR analysis, genomic DNA in total RNA samples was removed using TURBO™ DNase (Thermo Fisher Scientific) followed by purification with the Monarch RNA Clean Up Kit (NEB, Frankfurt, Germany). gDNA removal was assessed by PCR on chloroplast DNA followed by agarose gel electrophoresis. RNA was transcribed to cDNA using the Protoscript®II reverse transcriptase (NEB, Frankfurt, Germany). The Luna qPCR Mastermix (NEB, Frankfurt, Germany) was used for amplification on an 7500 Fast Real-Time PCR System (Applied Biosystems™).

Ribosome profiling

Isolation of ribosome footprints and total RNA

Wt Col-0 and *cp29a-6* plants were grown at 21°C 16/8hrs light/dark regime for 15 days and after this were transferred to cold conditions, 12°C 16/8hrs light/dark regime for three days. 350 mg frozen plant tissue was homogenized in liquid nitrogen with a

1109 mortar and pestle followed by the addition of 3.5 mL ribosome extraction buffer (0.2 M
1110 sucrose, 0.2 M KCl, 40 mM Tris-OAc pH 8.0, 10 mM MgCl2, 10 mM 2-
1111 Mercaptoethanol, 2% (v/v) polyoxyethylene (10) tridecyl ether, 1% (v/v) Triton X-100,
1112 100 µg/mL chloramphenicol, 100 µg/mL cycloheximide). After brief mixing, a 0.5 mL
1113 aliquot of the lysate was flash frozen and stored at -80 °C for later total RNA extraction
1114 using TRIzol reagent (ThermoFisher cat# 15596026). The remaining lysate was filtered
1115 through glass wool, followed by centrifugation for 10 min at 15,000 x g at 4 °C to
1116 remove cell debris. 3 mL of the clarified lysate were incubated with 1800 U of RNase I
1117 (Ambion cat# AM2294) for 1 h at room temperature with gentle rotation. The
1118 ribonuclease-treated lysate contains mainly monosomes which were loaded onto a 2
1119 mL sucrose cushion (30% (w/v) sucrose, 40 mM Tris-Acetate pH 8.0, 100 mM KCl, 15
1120 mM MgCl2, 0.1 mg/mL chloramphenicol, 0.1 mg/mL cycloheximide, 0.2% β-MeEtOH)
1121 and centrifuged (OptimaTM L-80 XP Ultracentrifuge - Beckman Coulter) for 1.5 h at
1122 303,800 x g at 4 °C. The supernatant was then aspirated and the pelleted monosomes
1123 resuspended in 0.5 mL footprint isolation buffer (10 mM Tris pH 8.0, 1 mM EDTA pH
1124 8.0, 100 mM NaCl, 1% (w/v) SDS, 0.1 M EGTA pH 8.0). The ribosome footprints were
1125 extracted from this pellet using 0.5 mL TRIzol reagent.

1126 Next, ribosome footprints were size-selected through electrophoresis on a 12%
1127 denaturing polyacrylamide gel (19:1, acrylamide:bisacrylamide) prepared in 1x TBE
1128 buffer (89 mM Tris, 89 mM Boric Acid, 2mM EDTA pH 8.0) containing 8 M urea. To
1129 this end, Approximately 60 µg ribosome footprints were resuspended in 100 µL of
1130 ribosome footprint loading buffer (90% (v/v) deionized formamide, 20 mM Tris-HCl pH
1131 7.5, 20 mM EDTA pH 8.0, 0.04% (w/v) bromophenol blue, and 0.04% (w/v) xylene
1132 cyanol) and denatured for 10 min at 70 °C. The gel was run in 1x TBE buffer with a
1133 constant power of 30 W at constant temperature of 12 °C (achieved by a cooling unit).
1134 Co-migrating pre-stained RNA ladder (Biodynamics Laboratory cat# DM253) was used
1135 to visualize the regions of the gel to excise ribosome footprints (20-40 nt). Ribosome
1136 footprints were eluted from the excised gel piece in 16 mL TESS (10 mM Tris pH 8.0,
1137 1 mM EDTA pH 8.0, 0.1 M NaCl, 0.2% (w/v) SDS) by overnight incubation at 4 °C with
1138 gentle rotation. Eluted ribosome footprints were isolated with 16 mL of
1139 phenol:chloroform:isoamyl alcohol (25:24:1), followed by overnight ethanol
1140 precipitation at -20 °C. To increase purity and further narrow the volume, the ribosome
1141 footprint pellet was resuspended in 0.1 M NaCl (500 µL) and subjected to a second
1142 round of phenol:chloroform:isoamyl alcohol (25:24:1) extraction, followed by two
1143 washes with chloroform:isoamylalcohol (24:1) and overnight ethanol precipitation at -
1144 20 °C. The received ribosome footprint pellet was washed twice with 75% ethanol and
1145 resuspended in RNase-free water.

rRNA depletion of ribosome footprints

1147 Oligo hybridization was performed following an adapted protocol from (Kraus et al.,
1148 2019). 150 ng gel-purified ribosome footprints were mixed with the following
1149 components in a PCR tube: 4 µL deionized formamide, 1 µL 20X SSC (3M NaCl, 0.3M
1150 Na-Citrate, pH 7.0 with HCl), 2 µL EDTA (5 mM, pH 8.0), 0.7 µL biotinylated oligo mix
1151 (100 µM, see table S4), and RNase free water up to 20 µL. Hybridization of the oligos
1152 was performed in a thermocycler with heated lid using a slow temperature ramp
1153 according to the table below:

Temp (°C)	80	75	70	65	60	55	50	45	40	35

Time (min)	5	2	2	2	2	2	2	2	2	2
Ramp rate	-0.1°C/s									

1154 After oligo hybridization, each sample was topped off to 40 µL using a solution of 1X
1155 SCC and 20% formamide and kept at 35 °C until ready for oligo removal, which was
1156 performed using Dynabeads MyOne C1 (Thermo Fisher cat# 65002). For each
1157 sample, 45 µL of beads were washed according to the manufacturer's protocol for RNA
1158 applications, and divided into 30 µL and 15 µL aliquots for performing two rounds of
1159 oligo removal. Each sample was incubated with the 30 µL bead aliquot at room
1160 temperature for 15 min, and magnetized for 2 min. The second round of oligo removal
1161 was performed by aspirating the supernatant into the 15 µL bead aliquot and repeating
1162 the incubation and magnetization. The final supernatant contains the rRNA-depleted
1163 ribosome footprints, which was aspirated, transferred into a clean tube and ethanol
1164 precipitated overnight at -20 °C. The rRNA-depleted ribosome footprint pellet was
1165 resuspended in RNase-free water and treated with TURBO DNase (Thermo cat#
1166 AM2238) according to the manufacturer's instructions, in order to remove traces of
1167 leftover DNA oligos. Following DNase treatment, ribosome footprints were purified
1168 using the Monarch RNA cleanup kit (NEB cat# T2030) following the modified protocol
1169 for small RNA.

1170 **Ribo-seq and RNA-seq library construction**

1171 To prepare the terminal ends for adapter ligation, rRNA-depleted ribosome footprints
1172 were treated with T4 polynucleotide kinase (PNK; ThermoFisher, cat#EK0031). The
1173 end-repaired ribosome footprints were purified using the Monarch RNA cleanup kit
1174 using the modified protocol for small RNA. These purified ribosome footprints were
1175 used as input for the NEXTflex small RNA-seq kit v3 (Perkin Elmer, cat# NOVA-5132-
1176 06). The resulting cDNA was amplified by 11-16 cycles of PCR with a barcode
1177 incorporated in the primer, and purified according to the instructions of the NEXTflex
1178 kit. For RNA-seq, 10 µg of purified total RNAs as described above were subjected to
1179 DNase treatment (TURBO DNase, Thermo cat# AM2238) following the manufacturer's
1180 instructions. The concentration of purified total RNA was quantified using a Qubit HS
1181 RNA assay (Thermo Fisher Scientific; Q32852). Then, 500 ng of purified total RNA
1182 were used to construct sequencing libraries using the Zymo-Seq RiboFree total RNA
1183 library kit (Zymo cat# R3000/R3003), which contains a step of an enzymatic
1184 degradation of rRNAs. Libraries were pooled for single-end 100-bp sequencing in a
1185 NovaSeq 6000 machine.

1186 Bioinformatic analysis was done by using the RiboDoc pipeline (François et al., 2021),
1187 which features the riboWaltz package (Lauria et al., 2018) for p-site estimation and
1188 quality controls.

1189 **DATA AND CODE AVAILABILITY**

1190 All data were analyzed using RStudio and Excel. Statistical tests, p values, number of
1191 biological and technical replicates, and number of independent experiments are
1192 indicated in the figure legends or main text. All RNA-Seq and Ribo-Seq data are

available at SRA, bioproject accession PRJNA981550. Reviewer link prior to publication:

https://dataview.ncbi.nlm.nih.gov/object/PRJNA981550?reviewer=1crku8tl9crm8itiiqd3sl742b

NMR data are deposited at BMRB with the ID 52022 and 52025.

References

Alberti, S. and Hyman, A.A. (2021). Biomolecular condensates at the nexus of cellular stress, protein aggregation disease and ageing. Nat. Rev. Mol. Cell Biol. 22: 196–213.

Antonicka, H., Sasarman, F., Nishimura, T., Paupe, V., and Shoubridge, E.A. (2013). The mitochondrial RNA-binding protein GRSF1 localizes to RNA granules and is required for posttranscriptional mitochondrial gene expression. Cell Metab. 17: 386–398.

Antonicka, H. and Shoubridge, E.A. (2015). Mitochondrial RNA Granules Are Centers for Posttranscriptional RNA Processing and Ribosome Biogenesis. Cell Rep. 10: 920–932.

Baker, N.A., Sept, D., Joseph, S., Holst, M.J., and McCammon, J.A. (2001). Electrostatics of nanosystems: application to microtubules and the ribosome. Proc. Natl. Acad. Sci. U. S. A. 98: 10037–10041.

Bobik, K., Fernandez, J.C., Hardin, S.R., Ernest, B., Ganusova, E.E., Staton, M.E., and Burch-Smith, T.M. (2019). The essential chloroplast ribosomal protein uL15c interacts with the chloroplast RNA helicase ISE2 and affects intercellular trafficking through plasmodesmata. New Phytol. 221: 850–865.

Borowski, L.S., Dziembowski, A., Hejnowicz, M.S., Stepien, P.P., and Szczesny, R.J. (2012). Human mitochondrial RNA decay mediated by PNPase–hSuv3 complex takes place in distinct foci. Nucleic Acids Res. 41: 1223–1240.

Burke, K.A., Janke, A.M., Rhine, C.L., and Fawzi, N.L. (2015). Residue-by-residue view of in vitro FUS granules that bind the C-terminal domain of RNA polymerase II. Mol. Cell 60: 231–241.

Castandet, B., Hotto, A.M., Strickler, S.R., and Stern, D.B. (2016). ChloroSeq, an Optimized Chloroplast RNA-Seq Bioinformatic Pipeline, Reveals Remodeling of the Organellar Transcriptome Under Heat Stress. G3 6: 2817–2827.

Chakrabortee, S., Kayatekin, C., Newby, G.A., Mendillo, M.L., Lancaster, A., and Lindquist, S. (2016). Luminidependens (LD) is an Arabidopsis protein with prion behavior. Proceedings of the National Academy of Sciences 113: 6065–6070.

Charollais, J., Dreyfus, M., and Iost, I. (2004). CsdA, a cold-shock RNA helicase from Escherichia coli, is involved in the biogenesis of 50S ribosomal subunit. Nucleic Acids Res. 32: 2751–2759.

Chen, D., Lyu, M., Kou, X., Li, J., Yang, Z., Gao, L., Li, Y., Fan, L.-M., Shi, H., and Zhong, S. (2022). Integration of light and temperature sensing by liquid-liquid phase separation of phytochrome B. Mol. Cell 82: 3015–3029.e6.

Chodasiewicz, M., Sokolowska, E.M., Nelson-Dittrich, A.C., Masiuk, A., Beltran, J.C.M., Nelson, A.D.L., and Skirycz, A. (2020). Identification and Characterization of the Heat-Induced Plastidial Stress Granules Reveal New Insight Into Arabidopsis Stress Response. Front. Plant Sci. 11: 595792.

Chotewutmontri, P. and Barkan, A. (2016). Dynamics of Chloroplast Translation during Chloroplast Differentiation in Maize. PLoS Genet. 12: e1006106.

Dammel, C.S. and Noller, H.F. (1995). Suppression of a cold-sensitive mutation in 16S rRNA by overexpression of a novel ribosome-binding factor, RbfA. Genes Dev. 9: 626–637.

Delaglio, F., Grzesiek, S., Vuister, G.W., Zhu, G., Pfeifer, J., and Bax, A. (1995). NMRPipe: a multidimensional spectral processing system based on UNIX pipes. J. Biomol. NMR 6: 277–293.

Dempsey, G.T., Vaughan, J.C., Chen, K.H., Bates, M., and Zhuang, X. (2011). Evaluation of fluorophores for optimal performance in localization-based super-resolution imaging. Nat. Methods 8: 1027–1036.

Dignon, G.L., Zheng, W., Kim, Y.C., and Mittal, J. (2019). Temperature-Controlled Liquid-Liquid Phase Separation of Disordered Proteins. ACS Cent Sci 5: 821–830.

Dong, X., Qu, G., Piazza, C.L., and Belfort, M. (2020). Group II intron as cold sensor for self-preservation and bacterial conjugation. Nucleic Acids Res. 48: 6198–6209.

Dupouy, G., McDermott, E., Cashell, R., Scian, A., McHale, M., Ryder, P., de Groot, J., Lucca, N., Brychkova, G., McKeown, P.C., and Spillane, C. (2022). Plastid ribosome protein L5 is essential for post-globular embryo development in Arabidopsis thaliana. Plant Reprod. 35: 189–204.

Emenecker, R.J., Holehouse, A.S., and Strader, L.C. (2020). Emerging Roles for Phase Separation in Plants. Dev. Cell 55: 69–83.

Fang, X., Wang, L., Ishikawa, R., Li, Y., Fiedler, M., Liu, F., Calder, G., Rowan, B., Weigel, D., Li, P., and Dean, C. (2019). Arabidopsis FLL2 promotes liquid–liquid phase separation of polyadenylation complexes. Nature 569: 265–269.

Farrow, N.A., Muhandiram, R., Singer, A.U., Pascal, S.M., Kay, C.M., Gish, G., Shoelson, S.E., Pawson, T., Forman-Kay, J.D., and Kay, L.E. (1994). Backbone dynamics of a free and phosphopeptide-complexed Src homology 2 domain studied by 15N NMR relaxation. Biochemistry 33: 5984–6003.

Félix, S.S., Laurents, D.V., Oroz, J., and Cabrita, E.J. (2023). Fused in sarcoma undergoes cold denaturation: Implications for phase separation. Protein Sci. 32: e4521.

Fernández-Suárez, M. and Ting, A.Y. (2008). Fluorescent probes for super-resolution imaging in living cells. Nat. Rev. Mol. Cell Biol. 9: 929–943.

Field, S., Jang, G.-J., Dean, C., Strader, L.C., and Rhee, S.Y. (2023). Plants use molecular mechanisms mediated by biomolecular condensates to integrate environmental cues with development. Plant Cell 35: 3173–3186.

Forman-Kay, J.D. and Mittag, T. (2013). From sequence and forces to structure, function, and evolution of intrinsically disordered proteins. Structure 21: 1492–1499.

François, P., Arbes, H., Demais, S., Baudin-Baillieu, A., and Namy, O. (2021). RiboDoc: A Docker-based package for ribosome profiling analysis. Comput. Struct. Biotechnol. J. 19: 2851–2860.

Franzmann, T.M. and Alberti, S. (2019). Prion-like low-complexity sequences: Key regulators of protein solubility and phase behavior. J. Biol. Chem. 294: 7128–7136.

Freeman Rosenzweig, E.S. et al. (2017). The Eukaryotic CO2-Concentrating Organelle Is Liquid-like and Exhibits Dynamic Reorganization. Cell 171: 148–162.e19.

Gao, Y., Thiele, W., Saleh, O., Scossa, F., Arabi, F., Zhang, H., Sampathkumar, A., Kühn, K., Fernie, A., Bock, R., Schöttler, M.A., and Zoschke, R. (2022). Chloroplast translational regulation uncovers nonessential photosynthesis genes as key players in plant cold acclimation. Plant Cell 34: 2056–2079.

Gueroussov, S., Weatheritt, R.J., O'Hanlon, D., Lin, Z.-Y., Narula, A., Gingras, A.-C., and Blencowe, B.J. (2017). Regulatory Expansion in Mammals of Multivalent hnRNP Assemblies that Globally Control Alternative Splicing. Cell 170: 324–339.e23.

Gutierrez-Beltran, E., Strader, L., and Bozhkov, P.V. (2023). Focus on biomolecular condensates. Plant Cell 35: 3155–3157.

Hajdukiewicz, P.T., Allison, L.A., and Maliga, P. (1997). The two RNA polymerases encoded by the nuclear and the plastid compartments transcribe distinct groups of genes in tobacco plastids. EMBO J. 16: 4041–4048.

Hanson, J., Paliwal, K., and Litfin, T. (2019). Enhancing protein intrinsic disorder prediction by utilizing deep squeeze and excitation residual inception and long short-term memory networks. Genomics Proteomics Bioinformatics 17: 645–656.

1288　Hoffmann, G., López-González, S., Mahboubi, A., Hanson, J., and Hafrén, A. (2023). Cauliflower mosaic
1289　　　virus protein P6 is a multivalent node for RNA granule proteins and interferes with stress granule
1290　　　responses during plant infection. Plant Cell 35: 3363–3382.

1291　Hofmann, S., Cherkasova, V., Bankhead, P., Bukau, B., and Stoecklin, G. (2012). Translation
1292　　　suppression promotes stress granule formation and cell survival in response to cold shock. Mol.
1293　　　Biol. Cell 23: 3786–3800.

1294　Huang, S., Zhu, S., Kumar, P., and MacMicking, J.D. (2021a). A phase-separated nuclear GBPL circuit
1295　　　controls immunity in plants. Nature 594: 424–429.

1296　Huang, X., Chen, S., Li, W., Tang, L., Zhang, Y., Yang, N., Zou, Y., Zhai, X., Xiao, N., Liu, W., Li, P.,
1297　　　and Xu, C. (2021b). ROS regulated reversible protein phase separation synchronizes plant
1298　　　flowering. Nat. Chem. Biol. 17: 549–557.

1299　Ivanov, P., Kedersha, N., and Anderson, P. (2019). Stress granules and processing bodies in
1300　　　translational control. Cold Spring Harb. Perspect. Biol. 11: a032813.

1301　Jones, P.G., Mitta, M., Kim, Y., Jiang, W., and Inouye, M. (1996). Cold shock induces a major ribosomal-
1302　　　associated protein that unwinds double-stranded RNA in Escherichia coli. Proc. Natl. Acad. Sci.
1303　　　U. S. A. 93: 76–80.

1304　Jourdain, A.A., Boehm, E., Maundrell, K., and Martinou, J.-C. (2016). Mitochondrial RNA granules:
1305　　　Compartmentalizing mitochondrial gene expression. J. Cell Biol. 212: 611–614.

1306　Jung, J.-H. et al. (2020). A prion-like domain in ELF3 functions as a thermosensor in Arabidopsis. Nature
1307　　　585: 256–260.

1308　Kang, H. and Xu, T. (2023). N6-methyladenosine RNA methylation modulates liquid–liquid phase
1309　　　separation in plants. Plant Cell 35: 3205–3213.

1310　Kato, M. et al. (2012). Cell-free formation of RNA granules: low complexity sequence domains form
1311　　　dynamic fibers within hydrogels. Cell 149: 753–767.

1312　Kearly, A., Nelson, A.D.L., Skirycz, A., and Chodasiewicz, M. (2022). Composition and function of stress
1313　　　granules and P-bodies in plants. Semin. Cell Dev. Biol.

1314　Kim, E.Y., Wang, L., Lei, Z., Li, H., Fan, W., and Cho, J. (2021). Ribosome stalling and SGS3 phase
1315　　　separation prime the epigenetic silencing of transposons. Nat Plants 7: 303–309.

1316　Klughammer, C. and Schreiber, U. (2008). Complementary PS II quantum yields calculated from simple
1317　　　fluorescence parameters measured by PAM fluorometry and the Saturation Pulse method. PAM
1318　　　application notes 1: 201–247.

1319　Kraus, A.J., Brink, B.G., and Siegel, T.N. (2019). Efficient and specific oligo-based depletion of rRNA.
1320　　　Sci. Rep. 9: 12281.

1321　Kroeger, T.S., Watkins, K.P., Friso, G., van Wijk, K.J., and Barkan, A. (2009). A plant-specific RNA-
1322　　　binding domain revealed through analysis of chloroplast group II intron splicing. Proc. Natl.
1323　　　Acad. Sci. U. S. A. 106: 4537–4542.

1324　Kupsch, C., Ruwe, H., Gusewski, S., Tillich, M., Small, I., and Schmitz-Linneweber, C. (2012).
1325　　　Arabidopsis chloroplast RNA binding proteins CP31A and CP29A associate with large transcript
1326　　　pools and confer cold stress tolerance by influencing multiple chloroplast RNA processing steps.
1327　　　Plant Cell 24: 4266–4280.

1328　Kusumi, K., Sakata, C., Nakamura, T., Kawasaki, S., Yoshimura, A., and Iba, K. (2011). A plastid protein
1329　　　NUS1 is essential for build-up of the genetic system for early chloroplast development under
1330　　　cold stress conditions. Plant J. 68: 1039–1050.

1331　Lancaster, A.K., Nutter-Upham, A., Lindquist, S., and King, O.D. (2014). PLAAC: a web and command-
1332　　　line application to identify proteins with prion-like amino acid composition. Bioinformatics 30:
1333　　　2501–2502.

1334　Lauria, F., Tebaldi, T., Bernabò, P., Groen, E.J.N., Gillingwater, T.H., and Viero, G. (2018). riboWaltz:
1335　　　Optimization of ribosome P-site positioning in ribosome profiling data. PLoS Comput. Biol. 14:
1336　　　e1006169.

1337　Lee, K. and Kang, H. (2020). Roles of Organellar RNA-Binding Proteins in Plant Growth, Development,
1338　　　and Abiotic Stress Responses. Int. J. Mol. Sci. 21.

1339   Li, C. and Fang, X. (2020). Phase Separation as a Molecular Thermosensor. Dev. Cell 55: 118–119.

1340   Liebers, M., Cozzi, C., Uecker, F., Chambon, L., Blanvillain, R., and Pfannschmidt, T. (2022). Biogenic
1341   signals from plastids and their role in chloroplast development. J. Exp. Bot. 73: 7105–7125.

1342   Lindquist, J.A. and Mertens, P.R. (2018). Cold shock proteins: from cellular mechanisms to
1343   pathophysiology and disease. Cell Commun. Signal. 16: 63.

1344   Liu, X., Rodermel, S.R., and Yu, F. (2010). A var2 leaf variegation suppressor locus, SUPPRESSOR
1345   OF VARIEGATION3, encodes a putative chloroplast translation elongation factor that is
1346   important for chloroplast development in the cold. BMC Plant Biol. 10: 287.

1347   Li, W., Hu, J., Shi, B., Palomba, F., Digman, M.A., Gratton, E., and Jiang, H. (2020). Biophysical
1348   properties of AKAP95 protein condensates regulate splicing and tumorigenesis. Nat. Cell Biol.
1349   22: 960–972.

1350   Li, Y.Q. and Sugiura, M. (1991). Nucleic acid-binding specificities of tobacco chloroplast
1351   ribonucleoproteins. Nucleic Acids Res. 19: 2893–2896.

1352   de Longevialle, A.F., Small, I.D., and Lurin, C. (2010). Nuclearly encoded splicing factors implicated in
1353   RNA splicing in higher plant organelles. Mol. Plant 3: 691–705.

1354   Majeran, W., Friso, G., Asakura, Y., Qu, X., Huang, M., Ponnala, L., Watkins, K.P., Barkan, A., and van
1355   Wijk, K.J. (2011). Nucleoid-enriched proteomes in developing plastids and chloroplasts from
1356   maize leaves: a new conceptual framework for nucleoid functions. Plant Physiol. 158: 156–189.

1357   Manalastas-Cantos, K. et al. (2021). ATSAS 3.0: expanded functionality and new tools for small-angle
1358   scattering data analysis. J. Appl. Crystallogr. 54: 343–355.

1359   McSwiggen, D.T., Mir, M., Darzacq, X., and Tjian, R. (2019). Evaluating phase separation in live cells:
1360   diagnosis, caveats, and functional consequences. Genes Dev. 33: 1619–1634.

1361   Molliex, A., Temirov, J., Lee, J., Coughlin, M., Kanagaraj, A.P., Kim, H.J., Mittag, T., and Taylor, J.P.
1362   (2015). Phase separation by low complexity domains promotes stress granule assembly and
1363   drives pathological fibrillization. Cell 163: 123–133.

1364   Nakamura, T., Ohta, M., Sugiura, M., and Sugita, M. (1999). Chloroplast ribonucleoproteins are
1365   associated with both mRNAs and intron-containing precursor tRNAs. FEBS Lett. 460: 437–441.

1366   Nakamura, T., Ohta, M., Sugiura, M., and Sugita, M. (2001). Chloroplast ribonucleoproteins function as
1367   a stabilizing factor of ribosome-free mRNAs in the stroma. J. Biol. Chem. 276: 147–152.

1368   Nott, T.J., Petsalaki, E., Farber, P., Jervis, D., Fussner, E., Plochowietz, A., Craggs, T.D., Bazett-Jones,
1369   D.P., Pawson, T., Forman-Kay, J.D., and Baldwin, A.J. (2015). Phase transition of a disordered
1370   nuage protein generates environmentally responsive membraneless organelles. Mol. Cell 57:
1371   936–947.

1372   Ouyang, M. et al. (2020). Liquid-Liquid Phase Transition Drives Intra-chloroplast Cargo Sorting. Cell
1373   180: 1144–1159.e20.

1374   Panchal, S.C., Bhavesh, N.S., and Hosur, R.V. (2001). Improved 3D triple resonance experiments, HNN
1375   and HN(C)N, for HN and 15N sequential correlations in (13C, 15N) labeled proteins: application
1376   to unfolded proteins. J. Biomol. NMR 20: 135–147.

1377   Pearce, S.F., Rebelo-Guiomar, P., D'Souza, A.R., Powell, C.A., Van Haute, L., and Minczuk, M. (2017).
1378   Regulation of Mammalian Mitochondrial Gene Expression: Recent Advances. Trends Biochem.
1379   Sci. 42: 625–639.

1380   Qamar, S. et al. (2018). FUS Phase Separation Is Modulated by a Molecular Chaperone and Methylation
1381   of Arginine Cation-π Interactions. Cell 173: 720–734.e15.

1382   Raab, S., Toth, Z., de Groot, C., Stamminger, T., and Hoth, S. (2006). ABA-responsive RNA-binding
1383   proteins are involved in chloroplast and stromule function in Arabidopsis seedlings. Planta 224:
1384   900–914.

1385   Rey, T., Zaganelli, S., Cuillery, E., Vartholomaiou, E., Croisier, M., Martinou, J.-C., and Manley, S.
1386   (2020). Mitochondrial RNA granules are fluid condensates positioned by membrane dynamics.
1387   Nat. Cell Biol. 22: 1180–1186.

Riback, J.A., Katanski, C.D., Kear-Scott, J.L., Pilipenko, E.V., Rojek, A.E., Sosnick, T.R., and Drummond, D.A. (2017). Stress-triggered phase separation is an adaptive, evolutionarily tuned response. Cell 168: 1028–1040.e19.

Richter, A.S., Nägele, T., Grimm, B., Kaufmann, K., Schroda, M., Leister, D., and Kleine, T. (2023). Retrograde signaling in plants: A critical review focusing on the GUN pathway and beyond. Plant Commun 4: 100511.

Roden, C. and Gladfelter, A.S. (2021). RNA contributions to the form and function of biomolecular condensates. Nat. Rev. Mol. Cell Biol. 22: 183–195.

Roy, S., Ueda, M., Kadowaki, K.-I., and Tsutsumi, N. (2010). Different status of the gene for ribosomal protein S16 in the chloroplast genome during evolution of the genus Arabidopsis and closely related species. Genes Genet. Syst. 85: 319–326.

Ruiz-Solaní, N. et al. (2023). Arabidopsis metacaspase MC1 localizes in stress granules, clears protein aggregates, and delays senescence. Plant Cell 35: 3325–3344.

Ruwe, H., Kupsch, C., Teubner, M., and Schmitz-Linneweber, C. (2011). The RNA-recognition motif in chloroplasts. J. Plant Physiol. 168: 1361–1371.

Sattler, M. (1999). Heteronuclear multidimensional NMR experiments for the structure determination of proteins in solution employing pulsed field gradients. Prog. Nucl. Magn. Reson. Spectrosc. 34: 93–158.

Schwenkert, S., Legen, J., Takami, T., Shikanai, T., Herrmann, R.G., and Meurer, J. (2007). Role of the low-molecular-weight subunits PetL, PetG, and PetN in assembly, stability, and dimerization of the cytochrome b6f complex in tobacco. Plant Physiol. 144: 1924–1935.

Shang, B. et al. (2023). Intrinsically disordered proteins SAID1/2 condensate on SERRATE for dual inhibition of miRNA biogenesis in Arabidopsis. Proc. Natl. Acad. Sci. U. S. A. 120: e2216006120.

Shen, Y. and Bax, A. (2013). Protein backbone and sidechain torsion angles predicted from NMR chemical shifts using artificial neural networks. J. Biomol. NMR 56: 227–241.

Shin, Y. and Brangwynne, C.P. (2017). Liquid phase condensation in cell physiology and disease. Science 357.

Small, I., Melonek, J., Bohne, A.-V., Nickelsen, J., and Schmitz-Linneweber, C. (2023). Plant organellar RNA maturation. Plant Cell 35: 1727–1751.

Solis-Miranda, J., Chodasiewicz, M., Skirycz, A., Fernie, A.R., Moschou, P.N., Bozhkov, P.V., and Gutierrez-Beltran, E. (2023). Stress-related biomolecular condensates in plants. Plant Cell 35: 3187–3204.

Tan, H., Luo, W., Yan, W., Liu, J., Aizezi, Y., Cui, R., Tian, R., Ma, J., and Guo, H. (2023). Phase separation of SGS3 drives siRNA body formation and promotes endogenous gene silencing. Cell Rep. 42: 111985.

Till, B., Schmitz-Linneweber, C., Williams-Carrier, R., and Barkan, A. (2001). CRS1 is a novel group II intron splicing factor that was derived from a domain of ancient origin. RNA 7: 1227–1238.

Ueda, M., Nishikawa, T., Fujimoto, M., Takanashi, H., Arimura, S.-I., Tsutsumi, N., and Kadowaki, K.-I. (2008). Substitution of the gene for chloroplast RPS16 was assisted by generation of a dual targeting signal. Mol. Biol. Evol. 25: 1566–1575.

Uniacke, J. and Zerges, W. (2009). Chloroplast protein targeting involves localized translation in Chlamydomonas. Proc. Natl. Acad. Sci. U. S. A. 106: 1439–1444.

Uniacke, J. and Zerges, W. (2008). Stress induces the assembly of RNA granules in the chloroplast of Chlamydomonas reinhardtii. J. Cell Biol. 182: 641–646.

Vranken, W.F., Boucher, W., Stevens, T.J., Fogh, R.H., Pajon, A., Llinas, M., Ulrich, E.L., Markley, J.L., Ionides, J., and Laue, E.D. (2005). The CCPN data model for NMR spectroscopy: development of a software pipeline. Proteins 59: 687–696.

Wang, A. et al. (2018a). A single N-terminal phosphomimic disrupts TDP-43 polymerization, phase separation, and RNA splicing. EMBO J. 37.

Wang, J. et al. (2018b). A Molecular Grammar Governing the Driving Forces for Phase Separation of Prion-like RNA Binding Proteins. Cell 174: 688–699.e16.

Wang, W. et al. (2023). The P-body component DECAPPING5 and the floral repressor SISTER OF FCA regulate FLOWERING LOCUS C transcription in Arabidopsis. Plant Cell 35: 3303–3324.

Wang, X., Wang, J., Li, S., Lu, C., and Sui, N. (2022). An overview of RNA splicing and functioning of splicing factors in land plant chloroplasts. RNA Biol. 19: 897–907.

Xie, D., Chen, M., Niu, J., Wang, L., Li, Y., Fang, X., Li, P., and Qi, Y. (2021). Phase separation of SERRATE drives dicing body assembly and promotes miRNA processing in Arabidopsis. Nat. Cell Biol. 23: 32–39.

Ye, L. and Sugiura, M. (1992). Domains required for nucleic acid binding activities in chloroplast ribonucleoproteins. Nucleic Acids Res. 20: 6275–6279.

Ying, Y., Wang, X.-J., Vuong, C.K., Lin, C.-H., Damianov, A., and Black, D.L. (2017). Splicing Activation by Rbfox Requires Self-Aggregation through Its Tyrosine-Rich Domain. Cell 170: 312–323.e10.

Yoo, S.-D., Cho, Y.-H., and Sheen, J. (2007). Arabidopsis mesophyll protoplasts: a versatile cell system for transient gene expression analysis. Nat. Protoc. 2: 1565–1572.

Yoshizawa, T. et al. (2018). Nuclear import receptor inhibits phase separation of FUS through binding to multiple sites. Cell 173: 693–705.e22.

Zavaliev, R., Mohan, R., Chen, T., and Dong, X. (2020). Formation of NPR1 Condensates Promotes Cell Survival during the Plant Immune Response. Cell 182: 1093–1108.e18.

Zhang, Y., Fan, S., Hua, C., Teo, Z.W.N., Kiang, J.X., Shen, L., and Yu, H. (2022). Phase separation of HRLP regulates flowering time in Arabidopsis. Sci Adv 8: eabn5488.

Zhao, C. and Pyle, A.M. (2017). Structural Insights into the Mechanism of Group II Intron Splicing. Trends Biochem. Sci. 42: 470–482.

Zoschke, R. and Bock, R. (2018). Chloroplast Translation: Structural and Functional Organization, Operational Control, and Regulation. Plant Cell 30: 745–770.

Zoschke, R., Watkins, K.P., and Barkan, A. (2013). A rapid ribosome profiling method elucidates chloroplast ribosome behavior in vivo. Plant Cell 25: 2265–2275.

Supplemental Data files

Figure S1: Sequence, structure and phase separation analysis of recombinant CP29A; related to figure 1

Figure S2: Small-angle X-ray scattering analysis of the PLD linker of CP29A; related to figure 2

Figure S3: Accumulation of CP29A variants in transgenic Arabidopsis lines, related to figure 3

Figure S4: Immunofluorescence analysis of CP29A during cold acclimation demonstrates an increase in granular CP29A structures in chloroplasts; related to figure 3

Figure S5: Principal component analysis and retrograde signaling defects revealed by RNA-Seq analysis of long-term cold-treated *cp29a* mutants; related to figure 4B

Figure S6: RNA-Seq analysis of *cp29a* complementation lines after 3 and 10 days in the cold; related to figure 4C-F

Figure S7: Quality check of ribosome profiling data of short-term cold-treated plants; related to figure 5.

Movie S1: Droplet formation and droplet fusion of mNG::CP29A in vitro; related to figure 1

1481 **Movie S2: Demixing of PLD domain of CP29A solution that had been kept in ice cold water and**
1482 **was slowly returned to room temperature; A four-minute film shortened to 16 seconds in time-**
1483 **lapse; related to figure 2**

1484